

**PALEOSEISMIC INVESTIGATION OF THE RELATIONSHIP OF EARTHQUAKE-
INDUCED LIQUEFACTION DEPOSITS TO DEFORMATION AT A SITE IN THE
NEW MADRID SEISMIC ZONE**

By

Can Guven

A thesis submitted to the Graduate Faculty of
Auburn University
in partial fulfillment of the
requirements for the Master of Science
Degree in Geology

Auburn, Alabama

August 7th, 2021

Keywords: Paleoseismology, earthquake-induced liquefaction, electrical resistivity tomography,
soil texture, radiometric age

Copyright 2021 by Can Guven

Approved by

Dr. Lorraine Wolf (Chair), Lawrence C. Wit Professor of Geosciences

Dr. Stephanie Rogers, Assistant Professor of Geosciences

Dr. Thorsten Knappenberger, Associate Professor of Crop, Soils and Environmental Sciences

ABSTRACT

Geophysical, geologic, and soil surveys were conducted at a site in the New Madrid seismic zone (NMSZ) to explore the relationship of fluvial sedimentary deposits to earthquake-induced liquefaction features, such as sand blows and sand dikes. The site was selected based on satellite imagery, which showed two light-colored elongate areas that were later identified as earthquake-induced sand blows oriented parallel to the east-west flowing Pemiscot Bayou. The study was aimed at establishing (1) the factors in fluvial environments that control the consequential location of the liquefaction features, and (2) the timing of their causative earthquakes. Detail logging of ditch exposures at the site revealed crosscutting relationships of the liquefaction features to the host sediments. Radiocarbon dating of organic samples taken from the exposures suggests that the liquefaction features resulted from an A. D. 900 +/- 150 yr New Madrid event. Data from electrical resistivity tomography (ERT) surveys performed along four profiles illuminated the subsurface stratigraphy of the study site. Soil samples collected from the surface and from auger holes, along with published interpretations of depositional units found in the site vicinity, were used to relate features in the electrical resistivity profiles to depositional units of the Pemiscot Bayou. Relationships recorded in the ditch exposures provided ground truth for the ERT interpretation. Based on the ERT, satellite, and empirical data, a model was developed that explains how fine-grained deposits, such as abandoned channel, natural levee, overbank, and possibly backswamp deposits, create relatively impermeable barriers when juxtaposed with or overlain upon coarse-grained deposits such as point bar and braided stream deposits and consequently guide the upward flow of liquefied sediments toward the surface. The model explains the observation that the sand blows at the site formed along the margins of abandoned channels of the Pemiscot Bayou. Findings from the study contribute to understanding

the factors in fluvial environments that control the location of liquefaction deposits and may help to predict which environments are most vulnerable to liquefaction during an earthquake.

ACKNOWLEDGMENTS

I would like to express my sincere gratitude to my advisor professor, Dr. Lorraine Wolf, who has provided me her utmost support throughout my education at Auburn. I am very grateful for her willingness to include me in her study group. I am very grateful to Dr. Martitia Tuttle for her generous support both in the field and analysis. She never spared her continuous contributions at every stage of my study. I also would like to thank Dr. Stephanie Rogers for her constant guidance and support. I would like to show my gratitude to Dr. Thorsten Knappenberger for his agreeing to be on the thesis committee. His presence and the directions he provided have given me a better understanding of soil sciences. I would like to express my gratitude to all the professors in the department who contributed to my degree. I thank every graduate student of the Department of Geosciences for their friendship. I would especially like to acknowledge my office mate, Steffen Matthews, who provided his support without hesitation. I would also like to thank Bishop Robbins for his assistance in the field and Marion Haynes for his kind friendship, good humor and assistance with our field project and logistics. I am especially thankful to my family for their kindness, patience and support throughout my education. Finally, I would like to indicate my appreciation to the Republic of Turkey, Ministry of National Education for sponsoring my master education, to General Directory of Mineral Research and Exploration institution for their support through my master's degree. I would also like to acknowledge partial funding for this thesis was provided through Auburn University's Internal Grant Program, the Geoscience Advisory Board, and the Southeastern Section of the Geological Society of America.

TABLE OF CONTENTS

ABSTRACT	ii
ACKNOWLEDGMENTS	iv
TABLE OF CONTENTS	v
LIST OF FIGURES	vii
LIST OF TABLES	xii
LIST OF ABBREVIATIONS	xiv
INTRODUCTION	1
BACKGROUND	6
Geologic and Tectonic Setting	6
Early to Late Paleozoic	6
Mesozoic to Present	7
Surface Geology	8
Ridges and Lowlands in the Lower Mississippi Valley	8
Pemiscot Bayou	11
Liquefaction Overview	11
Paleoseismological Studies	12
METHODOLOGY	15
Site Reconnaissance	15
Documenting Liquefaction Features	16

Dating Strategies	17
Geophysical Surveys	19
Soil Texture Analysis	21
Carbon Content Analysis	22
RESULTS	23
Liquefaction Features in the Outcrops	23
Geophysical Survey Results and Interpretations.....	27
ERT Data Set from the 2019 Field Visit	27
ERT Data Set from the 2020 Field Visit	30
Soil Texture Analysis	36
Auger Samples.....	36
Surface Soil Samples: Burnham Site.....	39
Surface Soil Samples: Bugg 40 and Dillahunty Sites.....	41
Timing of the Events	44
DISCUSSION.....	46
Factors Controlling Liquefaction at the Burnham Site	48
CONCLUSION.....	52
REFERENCES	54
APPENDIX A.....	62
APPENDIX B	65

LIST OF FIGURES

- Figure 1.** Topographic map of the study area with Reelfoot rift faults shown in solid black lines. The study area is marked by a black square. The dotted area indicates the distribution of earthquake-induced liquefaction along the NMSZ (modified from Saucier, 1977, 1994). Stars show the locations of 1811-1812 earthquakes; circles indicate earthquake epicenters recorded from 1811 to 2021 ($M \geq 2$; from CEUS-SSC (2015) and USGS (2021)). Abbreviations: RF, Reelfoot fault; AF, Axial fault; BCEF, Big Creek–Ellendale fault; CGL, Commerce geophysical lineament; EMF, Eastern Rift Margin fault; NMNF, New Madrid North fault; WMF, Western Rift Margin; NMWF, New Madrid West fault (modified from Thompson Jobe et al., 2020). 2
- Figure 2.** National Agriculture Imagery Program (NAIP) digital orthophotograph (July 2, 2010) of the Burnham (USDA, 2010) site outlined by black lines; Arrows point to linear and semi-circular to circular sand blows. The Pemiscot Bayou occupies the southern border of the study area. 5
- Figure 3.** Illustration showing the tectonic development of the Reelfoot rift and the Mississippi embayment with the passage of the Bermuda hot spot. (A) Rifting. (B) Emplacement of anomalous mantle. (C) Isostatic subsidence and failed rift. (D) Uplifting Ozark and Nashville domes and subsidence of the southern part of the embayment. (E) Intrusion of additional high-density masses into the upper crust (Bermuda hot spot). (F) Formation of present Mississippi embayment (modified from Braile et al., 1986; Cox and Van Arsdale, 2002). 8

Figure 4. Surface geology map of the Late Quaternary alluvial deposits in the Western Lowland and St. Francis Basin showing the locations of the Pemiscot Bayou and study area (modified from Obermeier, 1989; Guccione et al., 1999). 10

Figure 5. July 2, 2010, NAIP digital orthophotograph of the Burnham site (USDA, 2010). Solid yellow lines represent electrical resistivity tomography (ERT) profiles. Northern and southern ditch exposures are shown with red and black outlined triangles, respectively. Black outlined squares indicate the location of the auger samples. Black circles indicate surface soil sample locations; red circles indicate locations of soil samples from ditch exposures. Dashed white lines delineate the postulated abandoned channels of the Pemiscot Bayou. 16

Figure 6. Diagram illustrating the technique of collecting samples from liquefaction features and using these samples for age determination (Tuttle et al., 2019). 19

Figure 7. A) Photograph and interpretation of liquefaction features in northern ditch exposure at the Burnham site. The northern exposure is 1.2 m high and 2.5 m wide. B) Log of northern exposure with a detailed description of units and location of samples collected for radiocarbon dating. Sand dikes crosscut a buried soil. The exposure contains two distinct sand blows that could be the result of two separate earthquakes or two episodes within the same earthquake sequence. 25

Figure 8. A) Photograph and interpretation of liquefaction features in the southern ditch exposure. The exposure is 1 m high and 3.5 m wide. B) Log of southern exposure with a detailed description of units and location of sample collected for radiocarbon dating. A sand dike crosscuts a buried soil. As seen in the northern exposure, the southern exposure contains two distinct sand blows that could be the result of two separate earthquakes or two episodes within the same earthquake sequence. 26

Figure 9. Interpreted resistivity cross-section along the western ERT profile (Line A) at the Burnham site. See Figure 5 for location. Abbreviations: SB: Sand blow, SS: Source sand, AC: Abandoned channel fill deposit, L: Pemiscot Bayou levee deposit or overbank deposit, BSW: Backswamp deposit, B-st: Braided-stream deposit, PB: Point bar deposits. Arrows show possible pathways of vented sand blows. Dotted lines approximate interfaces of the braided-stream, point bar, and abandoned channel fill deposits. This figure includes relative locations of 14-m, 54-m, and 80-m auger sample depths in the enlarged portion. 28

Figure 10. The eastern ERT data (line B) at the study site. Abbreviations: SB: Sand blow, SS: Source sand, AC: Abandoned channel fill deposit, L: Pemiscot Bayou levee deposit or overbank deposit, BSW: Backswamp deposit, B-st: Braided-stream deposit, PB: Point bar deposits, (R): Ridge, (S): Swale. Arrows show possible pathways of vented sand blows. Dotted lines show approximate contacts between units. 28

Figure 11. ERT data from Line C1. This line runs parallel to Lines A and B of the previous year. L: Levee, PB: Pemiscot Bayou point bar deposits, (R): Ridge. See Figure 5 for location of profile. 31

Figure 12. ERT data from Line C2. The second segment from the 286-meter-long ERT profile. L: Levee, AC: Abandoned channel, PB: Pemiscot Bayou Point Bar Deposits, (R): Ridge, (S): Swale. See Figure 5 for location of profile. 31

Figure 13. ERT data from Line C3. The third extracted profile from the 286-meter-long ERT profile. L: Levee, AC: Abandoned channel, PB: Pemiscot Bayou Point Bar Deposits, (R): Ridge, (S): Swale, SB: Sand Blow. See Figure 5 for location of profile. 32

Figure 14. ERT data from Line C4. The low resistivity backswamp deposits are subsided and covered by a high resistivity unit, possibly denoting sand blow deposits. These appear as light-colored circular patches on the satellite imagery in Figure 5. SB: Sand Blow..... 32

Figure 15. ERT data from Line C5, the fifth extracted profile from the 286-meter-long ERT profile. L: Levee, PB: Pemiscot Bayou Point Bar Deposits, (R): Ridge, (S): Swale, SB: Sand Blow. The combination of low- and moderately high-resistivity areas along the surface are thought to reflect interbedded fine and coarse-grained sediments. See Figure 5 for location of profile..... 33

Figure 16. ERT data from Line C6, the final section of the 286-meter-long profile. AC: Abandoned Channel, PB: Pemiscot Bayou Point Bar Deposits, (R): Ridge, (S): Swale, SB: Sand Blow. The sand blow interpreted in the northern end of the profile is on strike with the sand blow observed in the southern ditch exposure. See Figure 5 for location. 33

Figure 17. Interpreted ERT profile (Line D) located closest to the current location of the Pemiscot Bayou. AC: Abandoned channel, PB: Pemiscot Bayou Point Bar Deposits, (R): Ridge, (S): Swale, SB: Sand blow, MRBSW: Mississippi River Backswamp Deposits, MR B-st: Mississippi River Braided Stream Deposits, L: Levee deposits. See Figure 5 for location. 35

Figure 18. Google Earth image of the Bugg 40 (A) and Dillahunty (B) sites (August 14, 2019), showing the locations of surface soil samples collected on both sand blow and host sediments. 42

Figure B-1. Particle size distribution graph of the sand grains of the Auger 120 sample. 65

Figure B-2. Particle size distribution graph of the sand grains of the Auger 150 sample. 66

Figure B-3. Particle size distribution graph of the sand grains of the Auger 1100 sample. 66

Figure B-4. Particle size distribution graph of the sand grains of the Auger 530 sample. 67

Figure B-5. Particle size distribution graph of the sand grains of the Auger 580 sample.	67
Figure B-6. Particle size distribution graph of the sand grains of the Auger 840 sample.	68
Figure B-7. Particle size distribution graph of the sand grains of the Auger 890 sample.	68
Figure B-8. Particle size distribution graph of the sand grains of the BURNS1-S sample.	69
Figure B-9. Particle size distribution graph of the sand grains of the BURNS2-S sample.	69
Figure B-10. Particle size distribution graph of the sand grains of the BURNS2-S sample.	70
Figure B-11. Particle size distribution graph of the sand grains of the BURSS1-S sample.	70
Figure B-12. Particle size distribution graph of the sand grains of the BURSS1-D sample.	71
Figure B-13. Particle size distribution graph of the sand grains of the BURAN sample.	71
Figure B-14. Particle size distribution graph of the sand grains of the BURAM sample.....	72
Figure B-15. Particle size distribution graph of the sand grains of the BURAS sample.	72
Figure B-16. Particle size distribution graph of the sand grains of the BUGS1 sample.....	73
Figure B-17. Particle size distribution graph of the sand grains of the BUGR1 sample.	73
Figure B-18. Particle size distribution graph of the sand grains of the DILS1 sample.	74
Figure B-19. Particle size distribution graph of the sand grains of the DILS2 sample.	74
Figure B-20. Particle size distribution graph of the sand grains of the DILR1 sample.	75

LIST OF TABLES

- Table 1.** Soil texture and carbon content results of the auger samples. The first digit of the sample number refers to the sample location (see Figures 5 and 9). The remaining digits refer to the depth of the sample (cm). Their location relative to the ERT profile is given in Figure 9. Distribution of the sand grains and coordinates of the locations of the samples are given in the appendix section..... 38
- Table 2.** Soil texture and carbon content analysis results of the surface samples and the samples from the ditch exposures at the Burnham site. The first three letters of samples names refer the site (BUR for Burnham site). The fourth and fifth letters refer the location (NS: northern sand blow, SS: southern sand blow, AN: north of the abandoned ch., AM: middle of the abandoned ch., AS: south of the abandoned ch.). the sixth place is the sample number. Characters after dash are S for surface samples and D for the samples collected from the ditch exposure. Locations of the samples are shown in satellite image (Figure 5), and distribution of the sand grains and coordinates of the locations of the samples are given in the appendix section..... 40
- Table 3.** Soil texture and carbon content analysis results of the surface samples from the Bugg 40 site. The first three letters of samples names refer the site (BUG for Bugg 40 site). The fourth letter refers the location (S: sand blow, R: host sediment). The fifth place is the sample number. Locations of the samples are shown in satellite image (Figure 18A), and distribution of the sand grains and coordinates of the locations of the samples are given in the appendix section. 43
- Table 4.** Soil texture and carbon content analysis results of the surface samples from the Dillahunty site. The first three letters of samples names refer the site (DIL for Dillahunty site). The fourth letter refers the location (S: sand blow, R: host sediment). The fifth place is the sample number. Locations of the samples are shown in satellite image (Figure 18B), and

distribution of the sand grains and coordinates of the locations of the samples are given in the appendix section..... 43

Table A-1. Gravimetric water content and coordinates of the auger samples. 62

Table A-2. Gravimetric water content and coordinates of the surface and ditch exposure samples of the Burnham site. 63

Table A-3. Gravimetric water content and coordinates of the surface and ditch exposure samples of the Bugg 40 site. 63

Table A-4. Gravimetric water content and coordinates of the surface and ditch exposure samples of the Dillhunty site. 63

Table A-5. Distance and the coordinates of the ERT profiles. 64

LIST OF ABBREVIATIONS

AC	Abandoned Channel
AF	Axial Fault
BCEF	Big Creek–Ellendale fault
B-st	Braided Stream
B.P.	Before present
BSW	Backswamp
CEUS	Central Eastern United States
ch	channel
CGL	Commerce Geophysical Lineament
cm	centimeter
EMF	Eastern Rift Margin Fault
ERT	Electrical Resistivity Tomography
g	gram
L	Levee
M	Magnitude
m	meter

NAIP	National Agriculture Imagery Program
NMNF	New Madrid North Fault
NMSZ	New Madrid Seismic Zone
NMWF	New Madrid West Fault
PB	Point Bar
SB	Sand Blow
SS	Source Sand
SSC	Seismic Source Characterization
USGS	United States Geological Survey
WMF	Western Rift Margin
yr	Year

INTRODUCTION

The New Madrid seismic zone (NMSZ) is a seismically active zone in the central United States. Most seismicity in the zone occurs along the faults within the Reelfoot rift, a basement structure buried beneath sediments of the northern Mississippi embayment (Figure 1). The faults of the Reelfoot rift have produced large earthquakes with an approximate recurrence interval of 500 years and more frequent low-magnitude earthquakes (Johnston and Nava, 1985; Kelson *et al.*, 1996; Tuttle *et al.*, 2002; Wolf *et al.*, 2006). Even though large earthquakes in the NMSZ happen infrequently, they have the potential to cause extensive soil liquefaction and long-lasting damage in the states of Missouri, Kentucky, Tennessee, and Arkansas. The most well-known events in the NMSZ are three major earthquake sequences, with magnitudes (M) greater than 7, that occurred between December 1811 and February 1812. According to a risk analysis performed for the NMSZ, if an earthquake similar to those of the 1811-1812 events occurred today, it could result in approximately \$300 billion in direct economic losses with 86,000 casualties, 7.2 million displaced people and over two million people needing shelter, with Tennessee, Arkansas, and Missouri being the most affected states (Elnashai *et al.*, 2009). For this reason, knowledge of the earthquake history of the NMSZ is critical for assessing seismic hazard in this zone.

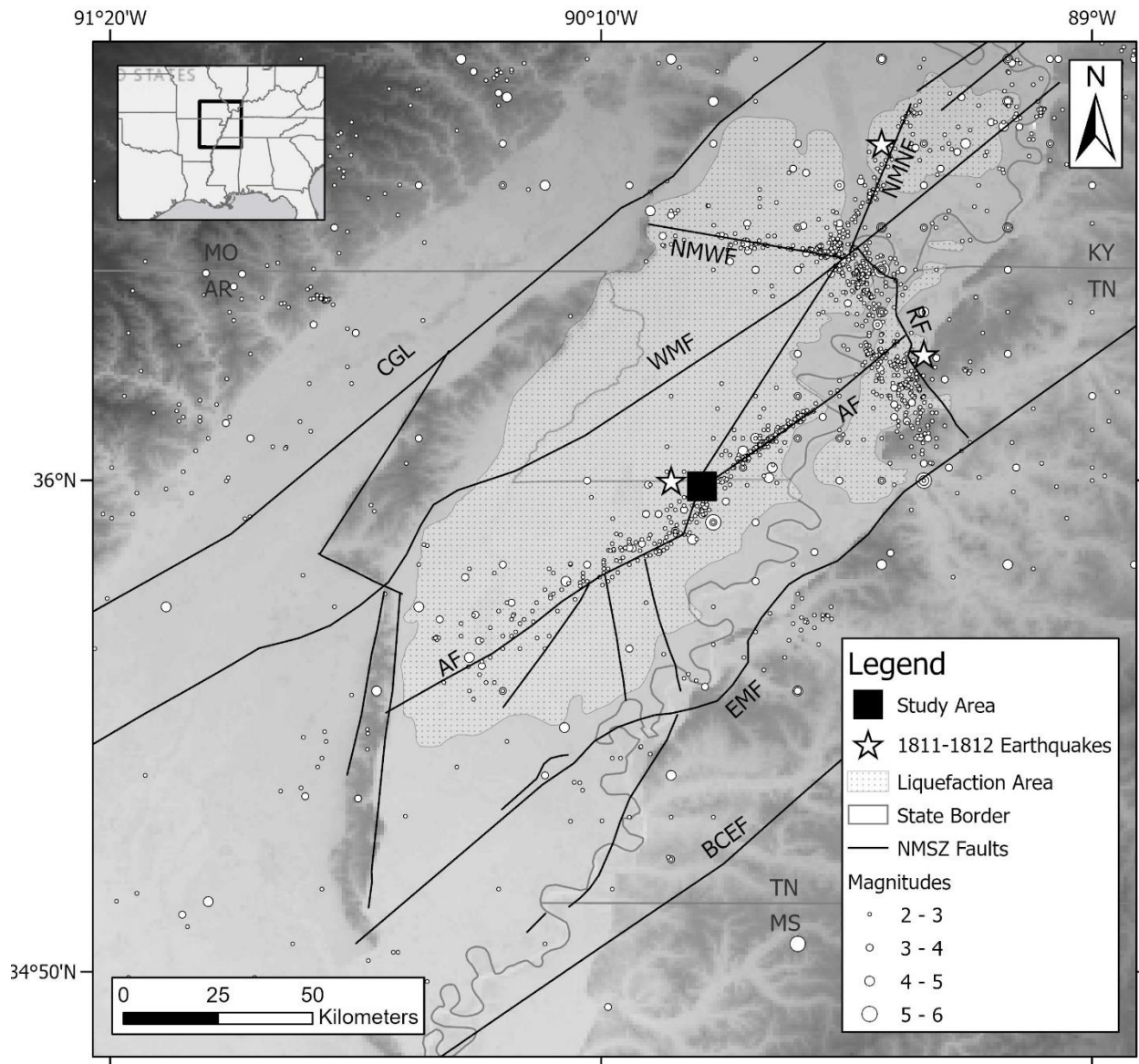


Figure 1. Topographic map of the study area with Reelfoot rift faults shown in solid black lines. The study area is marked by a black square. The dotted area indicates the distribution of earthquake-induced liquefaction along the NMSZ (modified from Saucier, 1977, 1994). Stars show the locations of 1811-1812 earthquakes; circles indicate earthquake epicenters recorded from 1811 to 2021 ($M \geq 2$; from CEUS-SSC (2015) and USGS (2021)). Abbreviations: RF, Reelfoot fault; AF, Axial fault; BCEF, Big Creek–Ellendale fault; CGL, Commerce geophysical lineament; EMF, Eastern Rift Margin fault; NMNF, New Madrid North fault; WMF, Western Rift Margin; NMWF, New Madrid West fault (modified from Thompson Jobe *et al.*, 2020).

Unlike other seismically active regions, the NMSZ lacks surface exposures of faulting.

Consequently, most of the knowledge of the earthquake history of the zone has come from

studies using proxy data, such as earthquake-induced liquefaction deposits. Paleoliquefaction, which is the study of soft-sediment deformation and soil liquefaction resulting from prehistoric earthquakes, has been an effective approach for unravelling the long-term behavior of the NMSZ. Earthquake-induced liquefaction results from increased porewater pressure due to rapidly applied and repetitive loading caused by earthquake waves (Owen, 1987; Tuttle *et al.*, 2019). During cyclic loading, water-saturated, loose granular sediments are rearranged, causing fluid pressure to build. Increased fluid pressure can then induce the upward flow of sediment-laden water, leading to the formation of liquefaction features, such as sand dikes, sand sills and sand blows (Tuttle *et al.*, 2019). Paleoliquefaction deposits are recognized as circular to semi-circular sand blows and linear, often *en echelon*, sand fissures (Tuttle *et al.*, 2019).

Paleoliquefaction studies have enabled the discovery of large, prehistoric earthquakes similar to the 1811-1812 events, and to date, more than 250 sites have been examined. Recently, Tuttle *et al.* (2019) suggested that the 500-year earthquake frequency occurrence may not have been constant over time and that there may have been a different earthquake recurrence time prior to 900 C.E. Because the occurrence of large earthquakes would have significant socio-economic effects in this region (Cramer, 2001; Elnashai *et al.*, 2009), it is important to understand its earthquake history and the conditions influencing soil liquefaction in an effort to prepare for future events.

This study is aimed at providing new knowledge of prehistoric earthquake occurrence at a site located near a prominent northeast-trending band of seismicity associated with the Axial fault (Figure 1). The site, herein referred to as the Burnham site, is an actively farmed property originally chosen as a potential location of prehistoric earthquake-induced liquefaction deposits based upon close examination of satellite images and site reconnaissance. The study site borders

the Pemiscot Bayou, a distributary of the Mississippi River. Satellite images show what appears to be multiple sand blows that are oriented subparallel to the current channel of the Pemiscot Bayou (Figure 2). This study sought to determine the approximate age of the earthquake that caused the liquefaction features at the site and the influence of fluvial depositional units on the location of the liquefaction features. The research questions addressed in this study are as follows: (1) Do the liquefaction features identified in the satellite imagery represent multiple generations of prehistoric earthquake events, and if so, what is their relative timing? (2) Are the locations of the liquefaction features at the site related to the distribution of fluvial depositional units? If so, what are the factors in fluvial environments that control the location of liquefaction deposits? The study uses electrical resistivity tomography (ERT) and soil sampling for constructing models of the subsurface stratigraphy, and detailed logging of liquefaction deposits in ditch exposures to evaluate the age of the deposits and the causative earthquake event.

It is hypothesized that the surface expression of sand blows was controlled by the distribution of fluvial sediments deposited by the Pemiscot Bayou and Mississippi River and their inherent physical properties, such as soil texture and permeability.

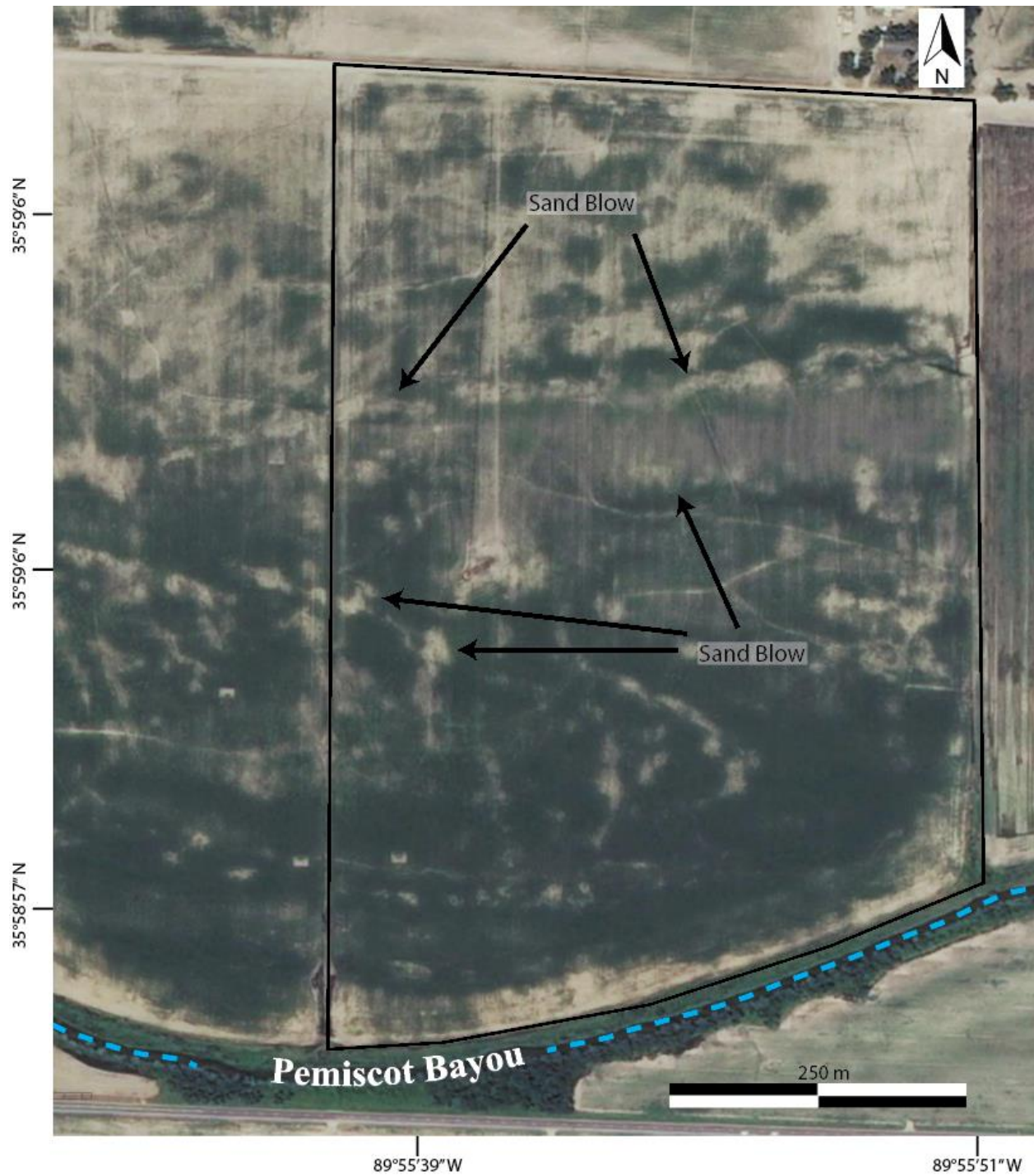


Figure 2. National Agriculture Imagery Program (NAIP) digital orthophotograph (July 2, 2010) of the Burnham (USDA, 2010) site outlined by black lines; Arrows point to linear and semi-circular to circular sand blows. The Pemiscot Bayou occupies the southern border of the study area.

BACKGROUND

Geologic and Tectonic Setting

The NMSZ is located in the Mississippi embayment, a southward-plunging trough containing over 1 km of Cretaceous and Cenozoic sediments overlain by Quaternary fluvial deposits (Cushing *et al.*, 1964; Hildenbrand *et al.*, 1977; Cox and Van Arsdale, 2002; Van Arsdale, 2009).

The embayment is the product of a long sequence of geologic events that began with Late Precambrian continental rifting related to the break-up of the supercontinent Rodinia and opening of the Iapetus Ocean (Ervin and McGinnis, 1975; Hildenbrand *et al.*, 1977; Mooney *et al.*, 1983; Thomas, 2006). Crustal extension was accompanied by igneous intrusion and volcanism (Ervin and McGinnis, 1975). Evidence for this process is a seismic high-velocity zone in the lower crust thought to reflect basaltic intrusion associated with the rifting, underlain by a low-velocity upper mantle (Pollitz and Mooney, 2014). Epeirogenic uplift accompanied the placement of low-density mantle material beneath the embayment (Figure 3A). Erosion ensued, leveling the surface of the rift, which failed to reach the full spreading stage (Ervin and McGinnis, 1975).

Early to Late Paleozoic

After the dispersion of the rifting forces, a large mass of mantle-derived magma intruded into the base of the crust and caused isostatic subsidence of the crust within the failed rift (Ervin and McGinnis, 1975). Subsidence enabled new sediments to be deposited above the rift structure and created the deep Reelfoot basin (Schwalb, 1969) (Figure 3B). Subsidence of the rift in combination with Taconic and subsequent Acadian orogenesis caused compressive stress on the rift zone and development of an inland seaway (Braile *et al.*, 1986) during which carbonates, and

marine Paleozoic clastic rocks were deposited above the Precambrian granites and dioritic gneisses of the rift zone (Ervin and McGinnis, 1975) (Figure 3C).

Mesozoic to Present

Following the deposition of marine rocks onto the rift, a period of uplift and erosion began in the Mesozoic. Reactivation of faults during this time was associated with uplift of the rift and intrusion of plutons along rift margins (Braile *et al.*, 1986) (Figure 3D). Reactivation during the mid-Cretaceous was thought to be influenced by the extensional tectonics dominating the Gulf Coastal Plain (Ervin and McGinnis, 1975; Braile *et al.*, 1986). Cox and Van Arsdale (2002), however, used stratigraphic evidence and reconstructions of the Bermuda hotspot track to argue that uplift and reactivation of the embayment was the result of increased heat flow from a superplume event. Faults associated with the formation of the rift served as conduits for mid-Cretaceous igneous intrusions. After the hot spot passed, the area subsided, and the upper Cretaceous units were deposited in the embayment graben (Cox and Van Arsdale, 2002) (Figure 3E). Relative subsidence and alluvial deposition continue to the present day, although data from geodetic studies suggests that there is little ongoing deformation (e.g., Gomberg and Ellis, 1994; Smalley *et al.*, 2005) (Figure 3F).

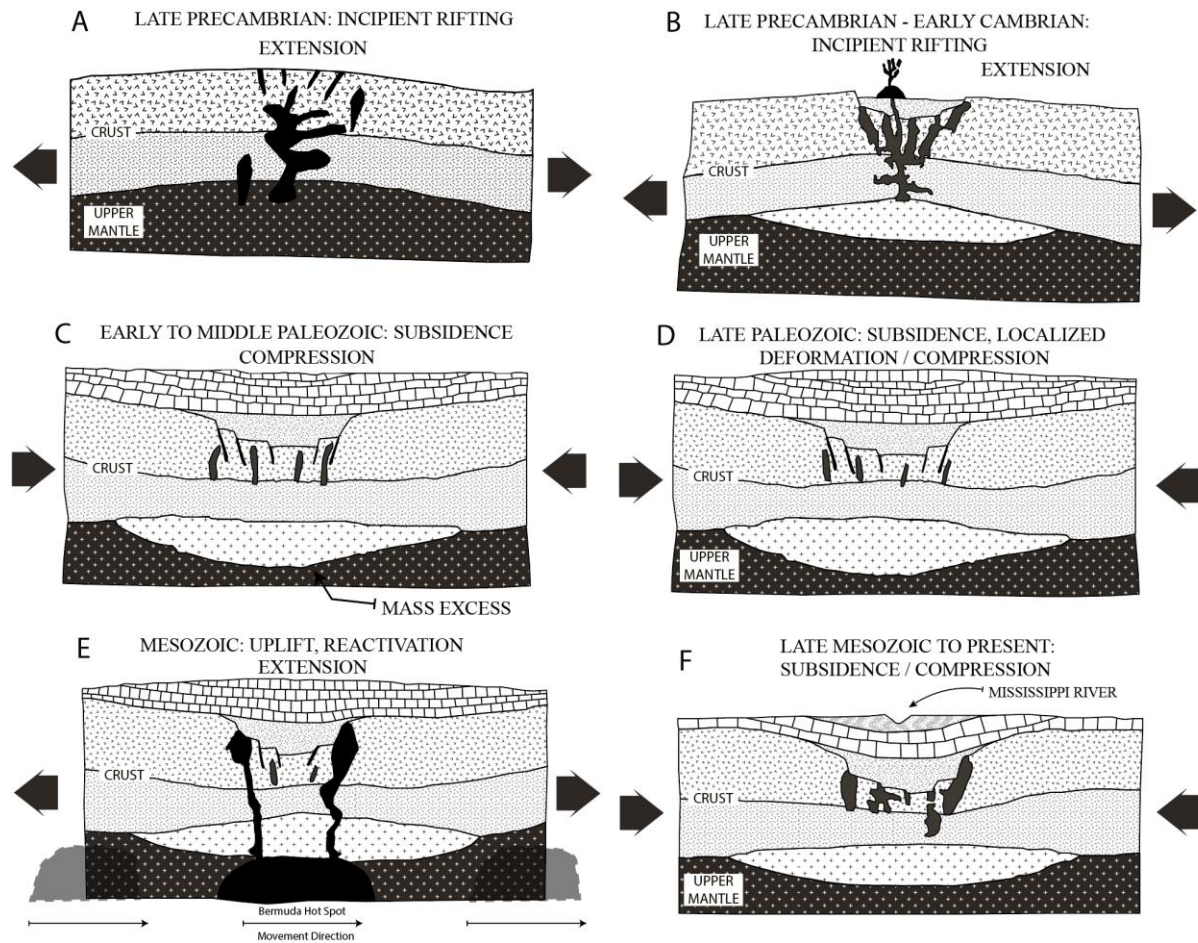


Figure 3. Illustration showing the tectonic development of the Reelfoot rift and the Mississippi embayment with the passage of the Bermuda hot spot. (A) Rifting. (B) Emplacement of anomalous mantle. (C) Isostatic subsidence and failed rift. (D) Uplifting Ozark and Nashville domes and subsidence of the southern part of the embayment. (E) Intrusion of additional high-density masses into the upper crust (Bermuda hot spot). (F) Formation of present Mississippi embayment (modified from Braile *et al.*, 1986; Cox and Van Arsdale, 2002).

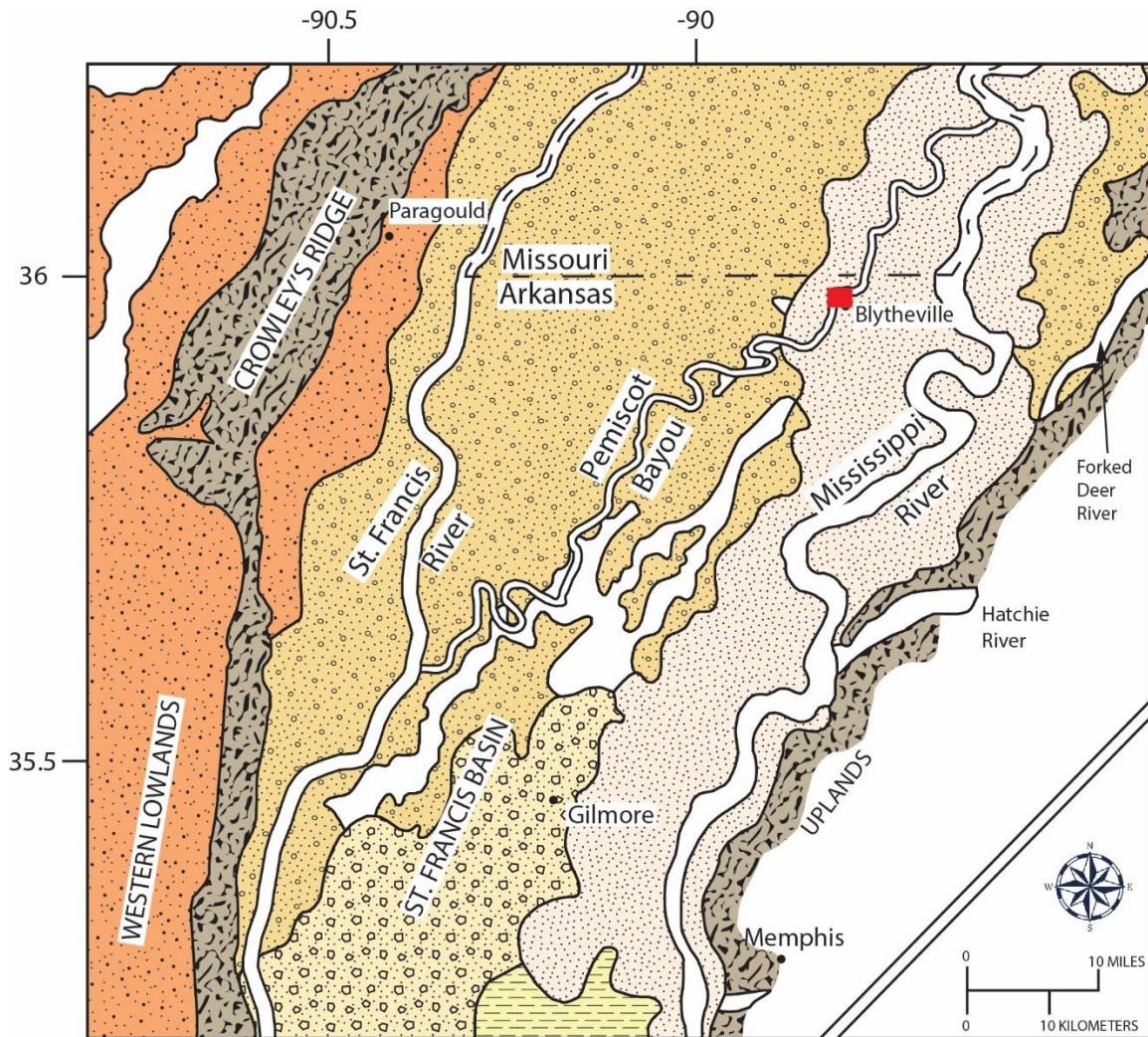
Surface Geology

Ridges and Lowlands in the Lower Mississippi Valley

The NMSZ encompasses the lowland portions of the northern Mississippi Embayment, which has been modified by fluvial processes associated with rivers from adjacent topographic highs, such as Sikeston Ridge and Crowley's Ridge (Obermeier, 1989) (Figure 4). As a major alluvial feature, Sikeston Ridge is a ~ 48 km long, north-south oriented topographic high formed

by Early Wisconsin Ohio River glacial outwash (Saucier, 1994). It took its final form by braided stream deposits that often rise as much as six meters above the adjacent plains on both sides (Obermeier, 1989). Crowleys Ridge is an upland that divides the Western lowlands and consists mostly of loess and gravel overlying semi-consolidated pre-Quaternary sediments (Obermeier, 1989). These topographic highs separate adjacent basins, such as St. Francis Basin and Western Lowlands (Saucier, 1964; Smith and Saucier, 1971) (Figure 4). The basins and lowlands are composed of natural levees, abandoned channels, and backswamp deposits (e.g., Saucier, 1964, 1994; Smith and Saucier, 1971; Obermeier, 1989). The Mississippi and the Ohio Rivers and their tributaries have formed the basins by fluvial erosion and deposition (Saucier, 1974).

Glacial meltwater discharge and sediments brought into the alluvial valley had an influence on the current meandering channel pattern of the Mississippi River (Guccione *et al.*, 1988; Royall *et al.*, 1991; Saucier, 1994). The Mississippi River valley now contains up to five different abandoned meander belts resulting from avulsions (Saucier, 1994).



Legend

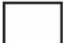







-  Alluvium on smaller streams
-  Present Mississippi River meander belt deposits
-  Older Mississippi River meander belt deposits
-  Backswamp deposits
-  Late Wisconsin braided-stream terraces of glacial outwash or valley train deposits
-  Early Wisconsin braided-stream terraces of glacial outwash or valley train deposits
-  Uplands
-  Study Area

Figure 4. Surface geology map of the Late Quaternary alluvial deposits in the Western Lowland and St. Francis Basin showing the locations of the Pemiscot Bayou and study area (modified from Obermeier, 1989; Guccione *et al.*, 1999).

Pemiscot Bayou

The Pemiscot Bayou is the youngest and the largest of the four distributaries found in the northern Lower Mississippi Valley (Figures 2 and 4) (Saucier, 1994). The Pemiscot Bayou has been studied extensively by Guccione *et al.* (1999), who assert that the Pemiscot Bayou was formed by the enlargement of a crevasse splay within the natural levee of the Mississippi River in southeastern Missouri that extended southward, where it eventually converged with the St. Francis River and ultimately rejoined the Mississippi River (Figure 4). The Pemiscot Bayou incorporated landforms such as point bar, natural levee, and abandoned channels, which are commonly associated with the meandering river systems. According to Guccione *et al.* (1999), the point-bar deposits consist of bedded fine to medium sand along the concave side of the channel, where natural levee deposits vary in grain size distribution along the channel. As the channel of the bayou becomes deeper, flooding events become relatively uncommon. Thus, they suggest that it is hard to distinguish the natural levee from overbank deposits. As the fluvial system evolves, the point bar sands can become buried under meters of silt to clayey silt. As this occurs, the depth of the channel becomes less, and flooding is more common. As a result, the natural levee can reach up to 3 meters of interbedded to massive silt, mud, and very fine sandy silt. Guccione *et al.* (1999) note that the width of natural levees can increase up to 10 km and can bury the point-bar sands of the bayou meander belt and adjacent Mississippi River backswamp clay. They claim that the present channel ceased to function as an active distributary and is largely infilled with interbeds of silt, sandy silt, and fine sand today.

Liquefaction Overview

Earthquake-induced liquefaction is a process during which saturated, loosely packed sand grains lose their strength during strong ground shaking (Seed and Idriss, 1982). Cyclic strains

caused by earthquake shaking can increase the porewater pressure to equal the total overburden pressure under confining conditions (Seed, 1979). The increased pressure is released as a slurry of sediment-laden water that flows toward the surface (Seed and Idriss, 1982). Sand from the source layer will eject into the topstratum through linear fissures or discrete vents (Saucier, 1994). Liquefaction during earthquakes is often associated with fluvial depositional units, such as point bar deposits, because of their high liquefaction susceptibility (Tuttle and Barstow, 1996; Tuttle, 2001).

Tuttle and Barstow (1996) reported that liquefaction within the braided stream deposits is guided by the orientation of the stream deposits and the thickness of the impermeable fine-grained sediment cap. They also noted that sand blows often develop parallel to the ridges of the point bar deposits. Giona Bucci *et al.* (2018) described liquefaction features that formed where (1) a point bar deposit was buried by a crevasse splay within an abandoned meander channel, and (2) a point bar deposit was buried by an active channel. The sand blow at the second location was controlled by two subtle ridges associated with the inside bend of the active river floodplain.

Paleoseismological Studies

Paleoseismological studies have been a key factor in establishing recurrence intervals of large earthquakes. Russ (1979) studied Late Holocene faulting and earthquake recurrence in the Holocene sediments at Reelfoot scarp. He found evidence suggesting at least two periods of faulting prior to the 1811 – 1812 New Madrid events. Based on these observations, he suggested a recurrence interval of ~ 600 yr or less in the past 2000 years for large earthquakes in the NMSZ. Johnston and Nava (1985) studied large earthquake recurrence by applying four different distribution functions (Gaussian, Lognormal, Weibull and Poisson) to tectonic data and seismological records. Based on these data, they suggested intervals of 550 years for $M > 7$, 254

years for $M > 6.6$, and 70 years for $M > 6$ earthquakes. Kelson *et al.* (1996) used geologic evidence from trench investigations to examine episodic deformation along the Reelfoot fault over the past 2400 years. They found three episodes of deformation between 780 and 1000 C.E., between 1260 and 1650 C.E., and 1812 C.E., respectively. Based on these findings, they estimated 400-500 years for the average recurrence interval for episodes of deformation caused by large earthquakes.

Paleoliquefaction studies, or studies of prehistoric earthquake-induced soil liquefaction, have become an effective approach in paleoseismological studies, especially where fault zones cannot be empirically observed. Based on many investigations of earthquake-induced liquefaction features in the NMSZ, Tuttle *et al.* (1999, 2002, 2005, 2019) established an earthquake chronology for the NMSZ, with large earthquake sequences occurring with an average frequency of approximately 500 years. These studies were based on radiocarbon and optically stimulated luminescence dating of samples acquired in trench excavations of liquefaction deposits or riverbank exposures of liquefaction features, such as sand dikes, blows and sills (Tuttle *et al.*, 1999, 2002, 2005, 2019; Gold *et al.*, 2019; Price *et al.*, 2019). In addition, dates were derived from Native American artifact collections preserved in occupation horizons discovered in association with liquefaction deposits. Based on these results, Tuttle *et al.* (2002) proposed large, prehistoric earthquakes in ~ 900 C.E. and 1450 C.E. Using the distribution of liquefaction deposits of similar age and the thickness of sand blows and their internal stratigraphy, they suggested that the 900 C.E. and 1450 C.E. earthquakes were associated with similar levels of ground shaking to that produced during the 1811–1812 earthquakes. Adding data from the southern part of the NMSZ, Tuttle *et al.* (2005) proposed the occurrence of

earthquakes in 2350 B.C.E. and 300 C.E., which were interpreted to be as large as the 1811-1812 earthquakes based on the large size of the liquefaction features.

Although previous findings supported the 500-year recurrence rate, the evidence for a large earthquake ~2350 B.C.E. suggests that either the earthquake record is incomplete, or the recurrence interval has changed through time. In more recent studies, (Tuttle *et al.*, 2019) revealed evidence for large earthquakes in ~ 0 C.E. and 1050 C.E. The new earthquakes, when added to the New Madrid earthquake chronology, support the possibility of a longer recurrence time prior to 0 C.E.; however, it is still recognized that the earthquake record, particularly of older events, is likely incomplete. The long-term earthquake behavior of the NMSZ will need additional study to reduce uncertainty in the timing of large events.

METHODOLOGY

Site Reconnaissance

Reconnaissance for suitable study sites involves targeting the possible locations of liquefaction features using satellite imagery or aerial photography. Liquefaction features appear on satellite images as light-colored circular, elliptical or linear patches on the ground surface (Obermeier, 1989; Tuttle and Barstow, 1996; Tuttle and Schweig, 1996; Tuttle *et al.*, 2019). Suitable sites are those that contain evidence of prehistoric sand blows. Distinguishing characteristics of prehistoric sand blows are deposits that are mottled, bioturbated, iron-stained, and/or cemented (Tuttle, 2010).

After selecting the Burnham site for further investigation, a field visit was arranged to examine and confirm possible sand blows seen in the satellite imagery (Figure 5). Test pits were dug in several locations that appeared to be sandier than the surrounding soil. The test pits revealed liquefaction features and confirmed the identification of the sand blow, as well as its relationship to the shallow underlying sedimentary deposits. Reconnaissance also included a survey of a drainage ditch bordering the site. Drainage ditches and river cut-banks offer an opportunity to observe the relationship of the liquefaction deposits to surrounding environments without trenching (Tuttle *et al.*, 2019).

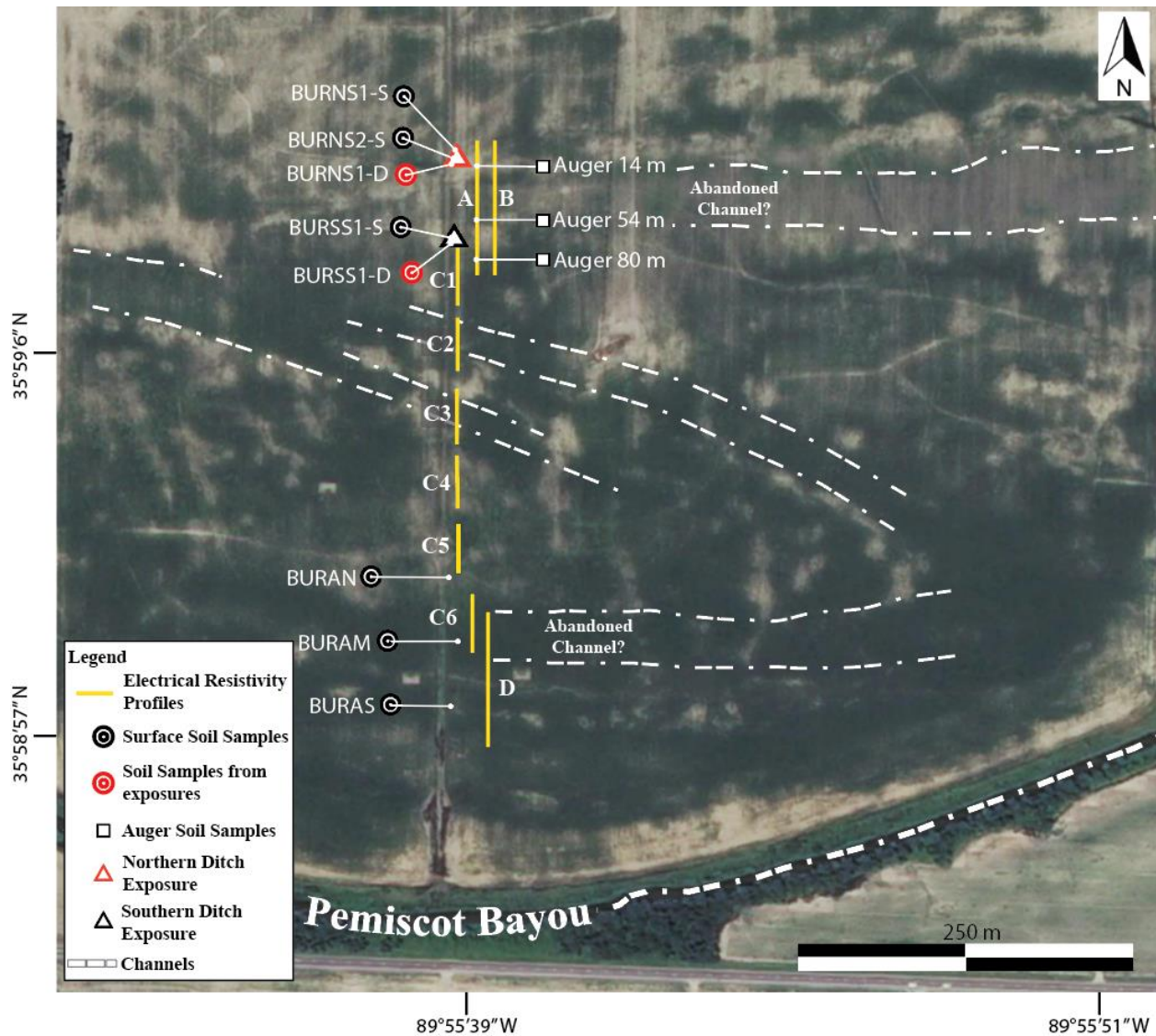


Figure 5. July 2, 2010, NAIP digital orthophotograph of the Burnham site (USDA, 2010). Solid yellow lines represent electrical resistivity tomography (ERT) profiles. Northern and southern ditch exposures are shown with red and black outlined triangles, respectively. Black outlined squares indicate the location of the auger samples. Black circles indicate surface soil sample locations; red circles indicate locations of soil samples from ditch exposures. Dashed white lines delineate the postulated abandoned channels of the Pemiscot Bayou.

Documenting Liquefaction Features

Two exposures of liquefaction features were discovered during reconnaissance of the drainage ditch. In preparation for close examination and detailed logging, the sidewall of the drainage ditch was scraped and cleaned to reveal feeder sand dikes connected to the sand blows

seen on the surface and to establish crosscutting relationships of the liquefaction features to the host sediments.

Exposures were logged using a 50-cm grid to allow for detailed documentation of sedimentological, stratigraphical, and structural relationships. Liquefaction features were described in terms of their sizes and orientations (width and orientation of the sand dikes and thickness of the sand blows), grain-size distributions, crosscutting relationships, and degree of soil development. The characteristics of the host sediments were also recorded. The cleaned ditch walls were then photographed. Both photographs and detailed logs of liquefaction features were later digitized using Adobe Illustrator™.

Dating Strategies

Understanding the timing of the liquefaction event is important for establishing a relationship with its causative earthquake(s). There are several tools and strategies for assessing the timing of the events, such as radiocarbon dating, crosscutting and stratigraphic relationships of features to host sediments, degree of soil development, and weathering characteristics. Radiocarbon dating of plant remains, such as leaves, seeds, roots or charcoal, is one of the most effective methods in determining the timing of events. Figure 6 illustrates how the timing of the liquefaction event is determined relative to the location of the sample and to crosscutting relationships in an exposure. The organic material within a soil horizon above a sand blow helps to determine the minimum age of the liquefaction. Organic material within a soil horizon buried by a sand blow provides a maximum age, or in cases where it is collected immediately below the contact with the sand blow, a close maximum approximate age. Other liquefaction features, such as sand dikes and sills, are not as effective in age determination because they are located deeper than the sand blow. Organic material within a deeper soil horizon will provide an older age than

the actual earthquake. Samples of organic material collected from stratigraphic zones that are in close spatial relationship to the liquefaction deposits provide the closest maximum and minimum age estimates (Tuttle, 2001; Tuttle *et al.*, 2019). In the absence of organic material appropriate for radiocarbon dating, stratigraphic location and crosscutting relationships of the liquefaction features to host sediments can provide relative ages related to the timing of the earthquake event. Host sediments provide maximum ages of the intruded sand (Tuttle *et al.*, 2019). For this study, five organic samples for radiocarbon dating were collected from the contact between the sand blows and the underlying soil horizons to estimate the timing of the burial. The locations of collected samples are shown in Figures 7 and 8. The samples were later examined under a microscope, and two selected samples were sent to Beta Analytic Inc. for radiocarbon dating.

Site investigations can reveal the degree of soil development and weathering characteristics of liquefaction features and can be used to distinguish older from younger sand blow deposits (Tuttle *et al.*, 2019). Climate, biological activity, topography, and time since deposition are some of the factors that play a role in soil development. A-horizon development or thickness in sand blows can be used to compare the relative age of sand blows. Similarly, the presence of soil lamellae in a deposit can be associated with sequential phases of sand blows and/or the transportation of materials from the topsoil with rainfall throughout time. Soil lamellae are defined as illuvial soil horizons having less than 7.5 cm thickness that are formed by the accumulation of silicate clay and/or by bridging sand and silt grains (Bockheim, 2014). The formation of soil lamellae in a sand blow can take hundreds to thousands of years, and its presence suggests that the sand blow is of prehistoric origin (Tuttle, 2001; Tuttle *et al.*, 2019). For this project, two soil samples from the ditch exposures and 7 auger samples were collected from the Burnham site. In addition, a total of 11 surface soil samples were collected from the

Burnham and two other nearby sites to examine the variation of soil development with respect to the time of sand blow formation.

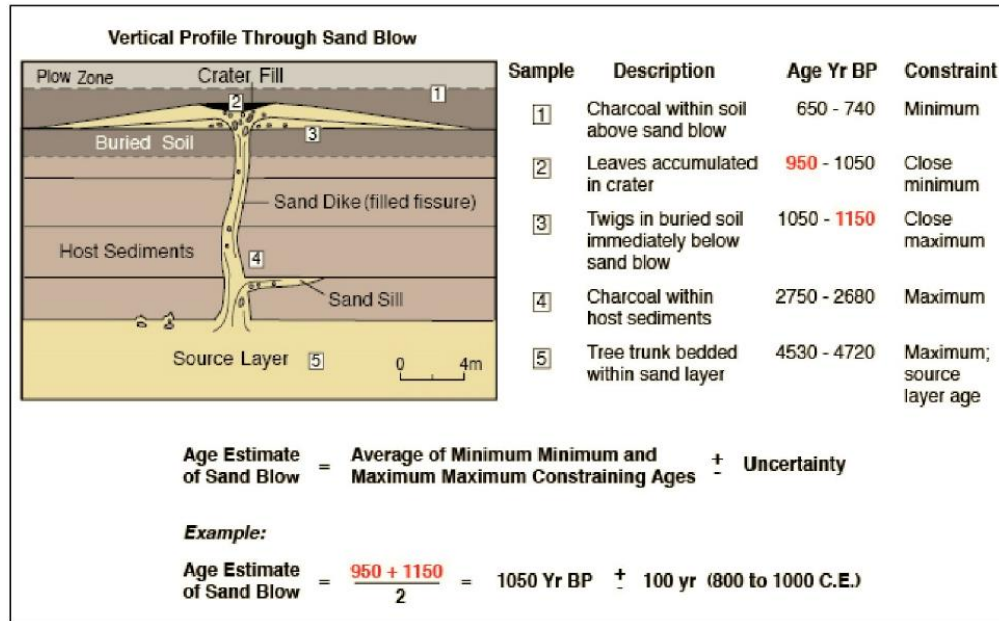


Figure 6. Diagram illustrating the technique of collecting samples from liquefaction features and using these samples for age determination (Tuttle *et al.*, 2019).

Geophysical Surveys

Geophysical methods, such as electrical resistivity tomography (ERT), are a non-invasive and effective means of illuminating the subsurface. Rocks and sediments have different physical properties that are reflected in measurements of their relative electrical resistivities. The resistivity of porous sediment is correlated with the degree of saturation and clay content (Ward, 1990). High values of apparent resistivity indicate coarse-grained materials, such as those associated with liquefaction deposits, whereas lower resistivity values are associated with fine-grained sediments, such as clay and silty-clay, which are characteristic of host sediments (Wolf *et al.*, 1998). Based on these differences, the depositional units at depth can be revealed by ERT.

For this research, ERT was performed along four profiles collected over two field visits to the Burnham site (Figure 5). During the first visit in 2019, data were collected along two 94-m north-south profiles oriented roughly perpendicular to a postulated abandoned channel and to two sand blows observed on the surface. The profile lines were positioned parallel to the ditch, crossing the eastward projection of the liquefaction features observed in the ditch exposure. Ideal locations for profiles are those that will locate feeder dikes connected to sand blows observed on the surface.

The ERT data were used in combination with the logs from the ditch exposures to evaluate the relationship of the liquefaction features to the fluvial depositional units. In 2020, a second ERT data set was collected using a roll-along method on a north-south profile (Figure 5). Although the intent was to create one long profile, errors in the data acquisition made some sections of the profile unusable. The useable data consist of short profile segments covering approximately 252 m of the original 286-m profile length. A third data set was collected along a 94-m north-south profile that overlapped the second data set and continued the line to the south, crossing another postulated abandoned channel of the Pemiscot Bayou (Figure 5).

The ERT survey was conducted using an Advanced Geosciences Inc. (AGI) Super Sting 48-electrode resistivity meter, and the data were processed with AGI EarthImager 2D™. All surveys utilized a dipole-dipole array with an a-spacing of 2 meters. The penetration depth varied with the length of the profiles and reached up to a maximum of 19 meters. The dipole-dipole array configuration in ERT is an effective method at detecting the lateral continuity of subsurface units and offers good resolution at shallow depths.

Soil Texture Analysis

Soil texture analyses were used to relate features in the ERT profile to depositional units. The results of the analysis, along with published interpretations of depositional units found in the site vicinity, were the basis for interpretation of the ERT data and relating these data to different types of fluvial sedimentary deposits (Kendall, 1997; Guccione *et al.*, 1999).

Samples from the surface, the ditch exposures and the subsurface were collected. Three soil samples were extracted from the ditch exposures, and a total of 11 samples were collected from the surface up to 24 cm in depth. Samples were chosen from both liquefaction deposits and from host sediments. The texture results of the surface samples were used to assess the degree of soil development in the liquefaction deposits. Auger samples were collected on the 14-m, 54-m, and 80-m positions on ERT profile Line A. The sample depths at the 14-m location were 20 cm, 50 cm, and 100 cm. The depths at the 54-m location were 30 cm and 80 cm. Lastly, the depths at the 80-m location were 40 cm and 90 cm. The auger locations relative to ERT profile Line A are shown in Figure 5 and relative depths of auger samples are described in "Soil Texture Analysis" section. The texture results of the auger samples are used in interpreting the ERT profiles in the context of the published literature (e.g., Kendall, 1997; Guccione *et al.*, 1999).

Soil texture is determined by particle size in terms of fractions of sand, silt, and clay particles within a sample (Gee and Or, 2002). These soil particles, especially silt and clay, are aggregated together and must be separated. The dispersion process consists of three methods: oxidative, chemical, and mechanical dispersion. For this study, all three dispersion methods were performed on the surface soil samples; however, only chemical and mechanical dispersion methods were used for the auger samples. Oxidative dispersion is the removal of organic material; 20 ml of hydrogen peroxide with a purity of 30% was added to a soil sample of 40 g in

four stages, once in the morning and then in the afternoon over two days. In chemical dispersion, sodium hexametaphosphate is used in a 5 g/L solution. This solution was placed on a shaker to separate particles mechanically for 24 hours.

Soil texture analyses were conducted using the hydrometer method and a set of five sieves. The hydrometer measurements were performed by placing a hydrometer in a tube with a total mixture of a one-liter solution of the soil with de-ionized water. The method relies on the concept of the buoyancy of the liquids. Soil particles in a liquid are suspended in accordance with their relative densities. As the particles settle over time, as determined by their specific gravity, the relative density of the liquid solution changes. The hydrometer instrument was used to measure the change in relative density of the liquid solution over time. The hydrometer measurements were collected at 0.5, 1, 3, 10, 30, 60, 90, 120, 1440 minutes. The material in the tube was then wet sieved to determine the amount of sand and sand fractions. The sieve apertures used were 1 mm, 0.5 mm, 0.25 mm, 0.1 mm, and 0.053 mm.

Carbon Content Analysis

One indication that a sand blow is prehistoric is the degree of soil development in the deposit. Carbon content is assumed to increase as the soil develops. Carbon content analysis was carried out to reveal the difference in soil development between samples taken from the sand blows and from the host sediments at the three different sites. Total carbon and organic carbon were measured using a Costech Combustion Elemental AnalyzerTM with an attached autosampler. Prior to analysis, samples were acidified for 12 hours in HCl vapors to remove inorganic carbon (Harris *et al.*, 2001).

RESULTS

Liquefaction Features in the Outcrops

Photographs and corresponding excavation logs of the two cutbank exposures examined at the Burnham site are shown in Figures 7 and 8, respectively. The exposures confirmed the presence of the liquefaction features that were related to the sand blows identified on the surface. The cleaned northern exposure was 1.2 m high by 2.5 m wide. The south exposure was 1 m high and 3.5 m wide. Preliminary examination of the northern and southern exposures revealed sand dikes crosscutting and sand blows overlying dark brown soil at both locations.

In the northern outcrop (Figures 7A and 7B), two dark brown sand dikes appear to crosscut a buried soil. The northern sand dike is approximately 15 cm wide, and the southern sand dike is approximately 50 cm wide, the latter trending N53°E and dipping 72°SE. The dip angle suggests that the source sand is located to the southeast of the exposure. The dikes are composed of fine-grained sand, with lesser amounts of medium- to fine-grained sand. The sand dike to the north contains a large soil clast, along with a few smaller soil clasts. The soil clasts likely belonged to the buried soil and were ripped from the buried soil by the upward movement of sediment-laden water and deposited along with the entrained sand along the bottom sand blow. One sand blow depositional unit overlies the other in the exposure. On the northern part of the outcrop, the sand dike is connected to the bottom sand blow and contains lignite, in addition to the soil clast around the vent area. It has approximately 25 cm of thickness. A medium-brown sand blow overlies the lower one, crossing the entire length of the exposure, with a thickness ranging from 25 to 70 cm. It reaches the maximum thickness over the southern sand dike and thins towards the north and south ends of the exposure. The upper sand blow contains large black to dark reddish-brown soil clasts, along with smaller clasts. The large soil clast in the northern

part of the exposure appears separated from a lower buried soil. The soil clast towards the south appears to be intact beneath the upper sand blow.

In the southern outcrop (Figure 8A and 8B), a dark, reddish-brown sand dike with a very fine to fine grain size is crosscutting very dark gray buried soil. The width of the dike is approximately 20 cm and trends N85°E and dips 13°N. The dip angle of the sand dike suggests that the location of the source sand is to the north of the sand blow. There is a visible amount of soil clasts just above the vent area towards the sand blows. The soil clasts were removed from the margin of the buried soil with the upward movement of sediment-laden water during an earthquake. Two depositional sand blow units were observed in the exposure. The first phase of the sand blow has a dark reddish-brown color and is underlain by a dark gray soil zone at the base and overlain by a dark yellowish-brown sand blow, which is a second phase of the sand blow. The first phase of sand blow is composed of fine- to medium-grained sand and has a clast-rich zone at the south end of the exposure. This unit is limited by a thin layer of silty sand on top that may indicate the waning stage of the earthquake. The second phase of the sand blow relates to the observed feeder sand dike, which crosscuts the first phase of the sand blow. We observed a couple of soil clasts around the vent area towards the sand blow that were most likely part of buried soil. The second phase the sand blow consists of medium- to fine-grained sand and has a clast zone above the vent area. The second phase of sand blow is ~ 80 cm thick near the sand vent and thins to ~ 10 cm towards the edges of the exposure. Both sand blows exhibit flow structures with grain size fining upwards.

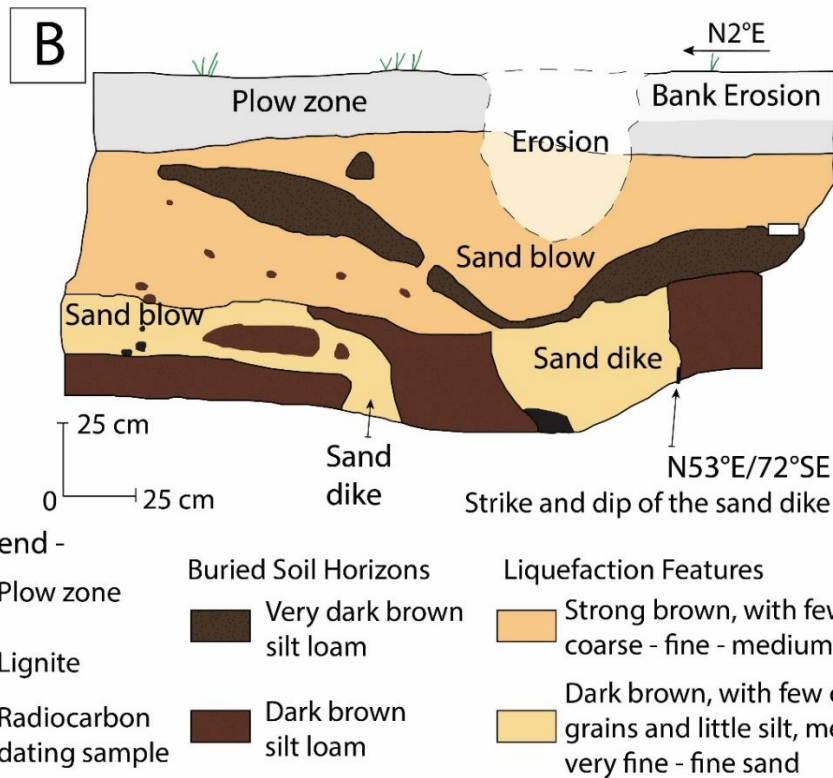
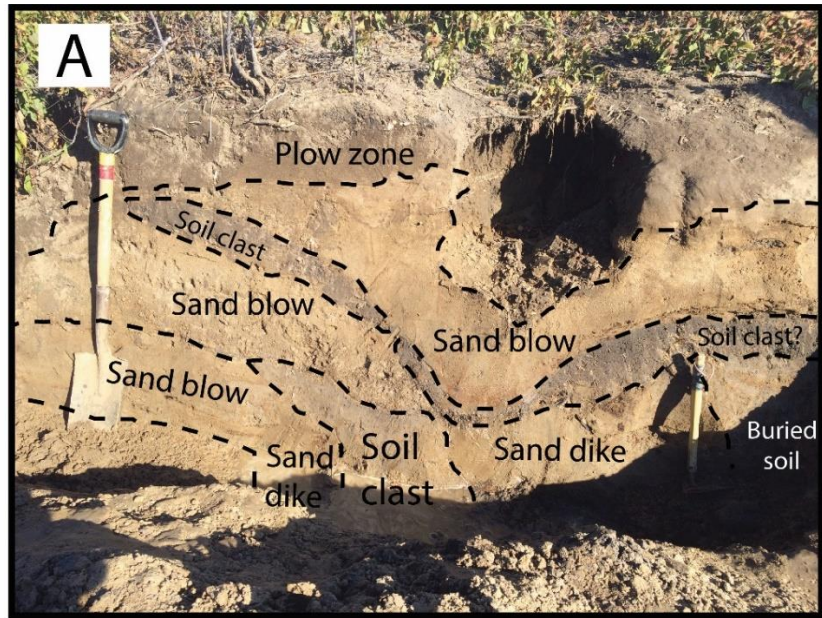


Figure 7. A) Photograph and interpretation of liquefaction features in northern ditch exposure at the Burnham site. The northern exposure is 1.2 m high and 2.5 m wide. B) Log of northern exposure with a detailed description of units and location of samples collected for radiocarbon dating. Sand dikes crosscut a buried soil. The exposure contains two distinct sand blows that could be the result of two separate earthquakes or two episodes within the same earthquake sequence.

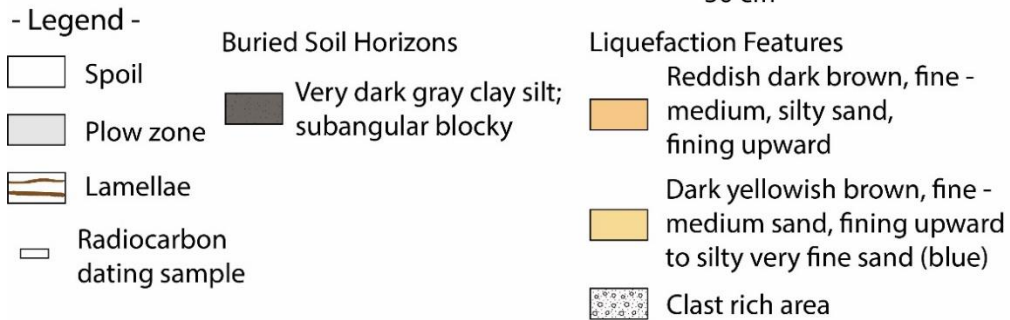
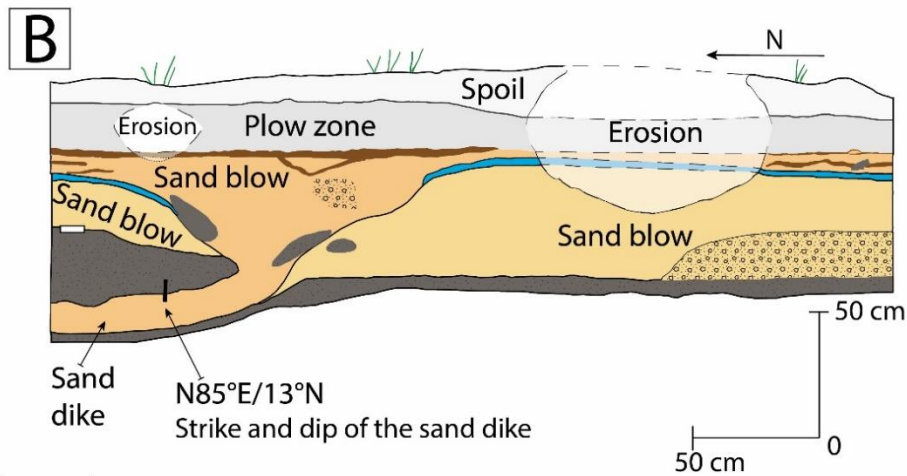
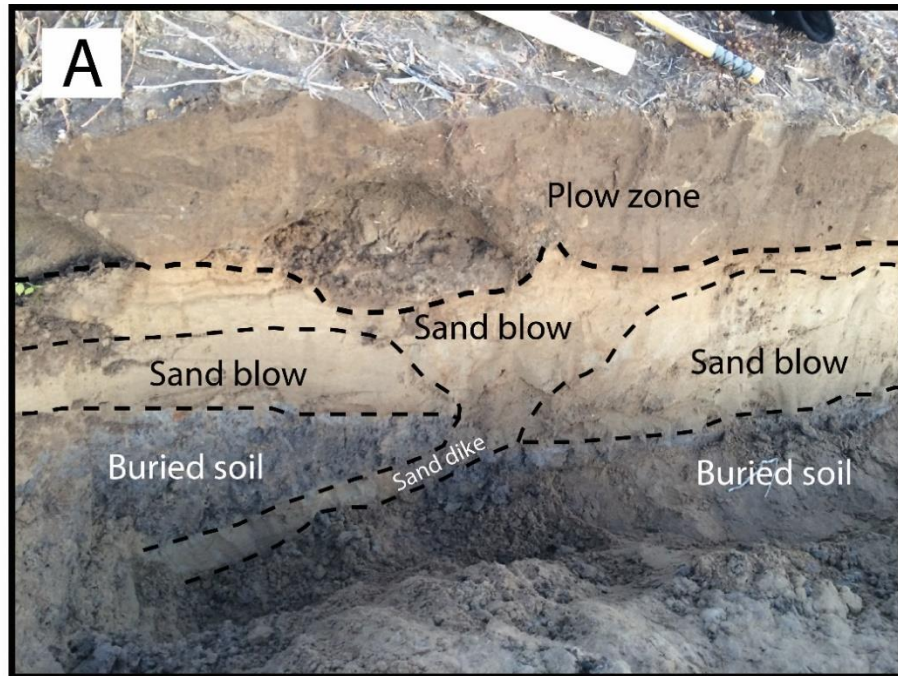


Figure 8. A) Photograph and interpretation of liquefaction features in the southern ditch exposure. The exposure is 1 m high and 3.5 m wide. B) Log of southern exposure with a detailed description of units and location of sample collected for radiocarbon dating. A sand dike crosscuts a buried soil. As seen in the northern exposure, the southern exposure contains two distinct sand blows that could be the result of two separate earthquakes or two episodes within the same earthquake sequence.

Geophysical Survey Results and Interpretations

ERT Data Set from the 2019 Field Visit

The ERT data set from the first field visit revealed the relationship of the subsurface stratigraphy to the surface deposits and the features seen in the ditch exposures. Two ERT profiles, Line A and Line B, are shown in Figures 9 and 10, respectively. In both profiles, lower relative resistivity values are associated with fine-grained sediments, such as clays and silts. Higher values are associated with coarse-grained sediments, such as sand. Along both profiles, coarse-grained units appear in the deeper depositional units.

Line A was positioned to be on strike with the sand blow deposit observed in the northern ditch exposure (Figures 5 and 9). A high-resistivity area between 6 m and 26 m from the northern end of the profile is correlated with the east-northeast-oriented sand blow seen on the surface (Figure 5) and observed in the northern ditch exposure. A possible feeder dike for the sand blow is located at approximately 18 m along the profile at 5 m depth. This moderately high resistivity feature crosscuts a low-resistivity zone, interpreted to be a fine-grained backswamp deposit. The dip of the interpreted dike is southeast, suggesting the location of source sand is in that direction and is consistent with the relationship observed in the ditch exposure. Below the low-resistivity zone, values transition to higher resistivities, which are consistent with a coarse-grained braided stream deposit, likely deposited by the Mississippi River. This unit is believed to be the source sand for the dike and the sand blow seen at the surface. Migration of the sand-laden water during liquefaction is denoted by the arrows.

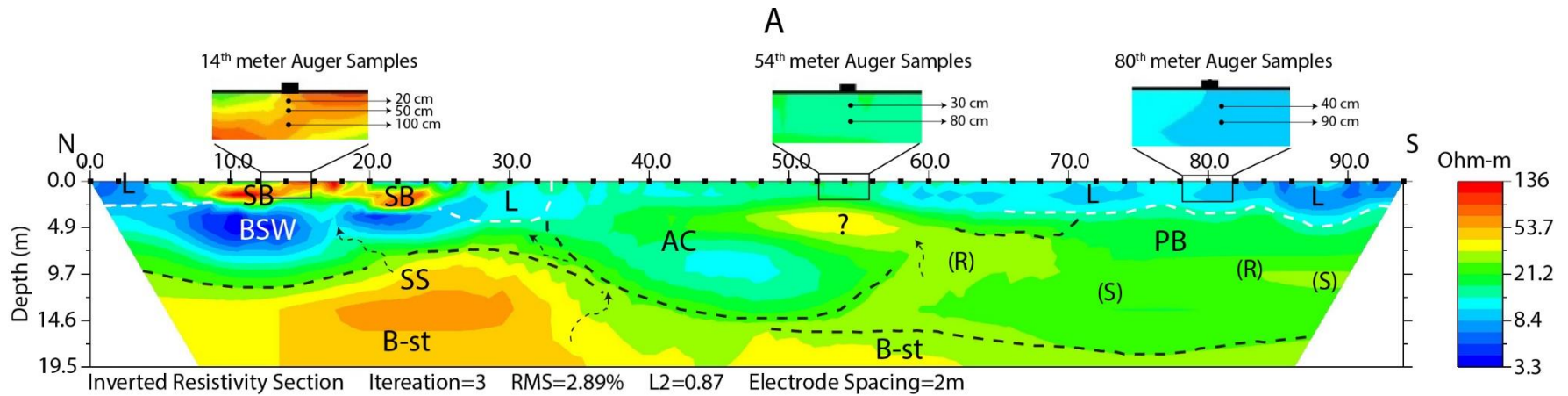


Figure 10. Interpreted resistivity cross-section along the western ERT profile (Line A) at the Burnham site. See Figure 5 for location. Abbreviations: SB: Sand blow, SS: Source sand, AC: Abandoned channel fill deposit, L: Pemiscot Bayou levee deposit or overbank deposit, BSW: Backswamp deposit, B-st: Braided-stream deposit, PB: Point bar deposits. Arrows show possible pathways of vented sand blows. Dotted lines approximate interfaces of the braided-stream, point bar, and abandoned channel fill deposits. This figure includes relative locations of 14-m, 54-m, and 80-m auger sample depths in the enlarged portion.

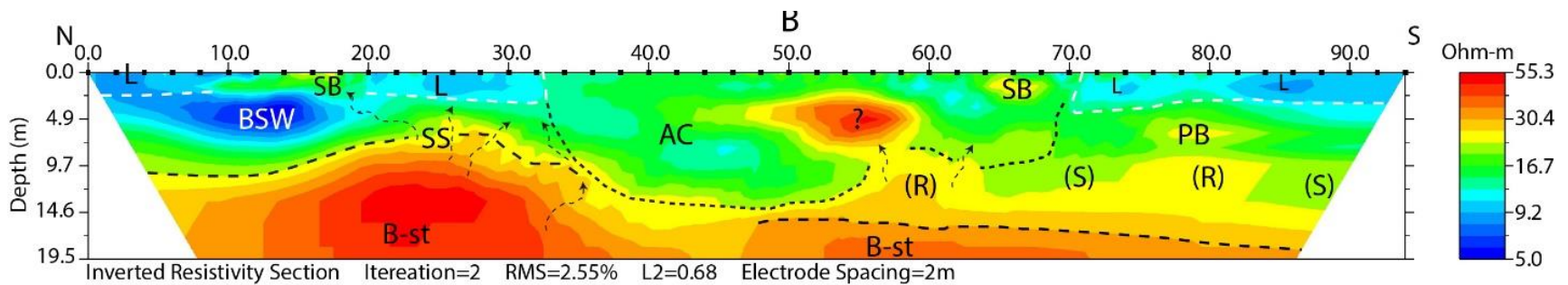


Figure 9. The eastern ERT data (line B) at the study site. Abbreviations: SB: Sand blow, SS: Source sand, AC: Abandoned channel fill deposit, L: Pemiscot Bayou levee deposit or overbank deposit, BSW: Backswamp deposit, B-st: Braided-stream deposit, PB: Point bar deposits, (R): Ridge, (S): Swale. Arrows show possible pathways of vented sand blows. Dotted lines show approximate contacts between units.

Line B captured the sand blow and liquefaction features at both northern and southern exposures (Figures 10). The sand blow observed in the southern exposure was projected to appear between 64 m and 68 m along the profile. As in Line A, an area of high resistivity towards the bottom of the profile is interpreted as a Mississippi River braided stream deposit (B-st). In the center of line B, low to average resistivity values above ~ 14 m depth are interpreted as a fine- to medium-grained deposit from an abandoned channel of the Pemiscot Bayou. This area appears on the satellite imagery as a dark to medium gray east-northeast trending linear band sandwiched between the north and south sand blow deposits (Figure 5). A high-resistivity area between 48 m and 58 m in the profile at ~ 5-m depth intrudes this area, suggesting a coarse-grained unit, possibly a liquefied sand deposit from an older earthquake or a liquefaction feature not seen at the surface in this cross-section location. An alternate interpretation is that the feature represents a coarse-grained unit such as a point bar deposit; however, its resistivity values are higher than other such features interpreted in the profiles. On the south end of the profile, higher resistivity areas located above the braided stream deposits may represent point bar deposits with ridge and swale structures. Low-resistivity values on both the north and south ends of the profile are interpreted as shallow fine-grained natural levee or overbank deposits. At the north end of the profile, the low-resistivity area beneath this unit and extending to ~18 m along the profile is interpreted as a silty, clayey backswamp deposit. The subsurface units identified on both ERT profiles agree with models of depositional units of the Pemiscot Bayou described by Kendall (1997) and Guccione *et al.* (1999).

ERT Data Set from the 2020 Field Visit

Two ERT data sets were collected during the second field visit in October 2020. The first ERT data set was acquired along 286-m north-south profile using a roll-along method. This profile started from approximately 19 m before the end of the 2019 ERT profile (Line A) and extended southward towards the current location of the Pemiscot Bayou.

Two problems occurred with data acquisition along the 286-meter-long profile (referred to here as Line C). The resulting salvageable data consist of 6 shorter line segments of ~ 40 m each (labelled C1-C6 in Figures 11-16). The locations of the corresponding segments are shown in Figure 5. Because the length of these lines is reduced, the imaging depths are also reduced. Interpretations of the subsurface units along these profile segments follow the same notations as in the previous profiles.

The first segment, Line C1, shows a thick (~ 4 m), low-resistivity area between ~ 4 m and 22 m along the profile that is interpreted as a fine-grained levee deposit (Figure 11). This low-resistivity area thins as it continues to the south. A higher resistivity area underlies this unit in the south half of the profile, indicating a much coarse-grained deposit, interpreted as a ridge or point bar deposit of the Pemiscot Bayou. To the south of Line C1, segment C2 (Figure 12) shows a broad, low-resistivity area that indicates fine-grained sediments interpreted as either a levee deposit or a smaller channel-fill deposit, similar to the abandoned channel-fill deposits. The undulating high-resistivity areas are possibly part of a swale and ridge point bar deposit. The high-resistivity area at the surface around 52 m in the profile may represent a sand blow deposit that is sourced from the high-resistivity unit below.

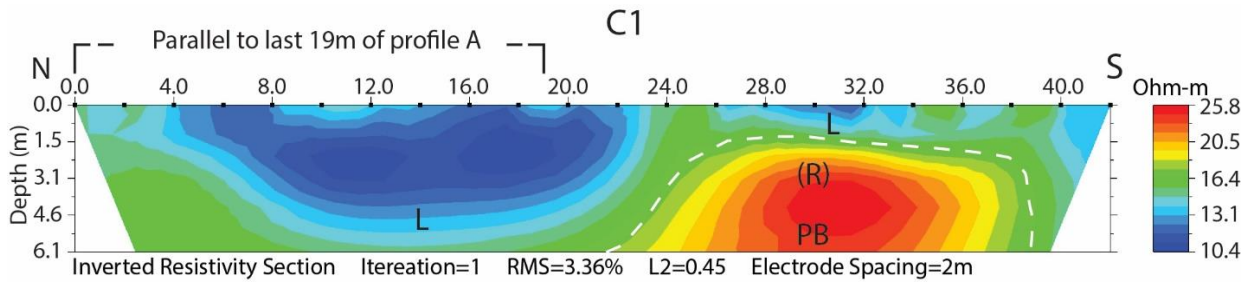


Figure 11. ERT data from Line C1. This line runs parallel to Lines A and B of the previous year. L: Levee, PB: Pemiscot Bayou point bar deposits, (R): Ridge. See Figure 5 for location of profile.

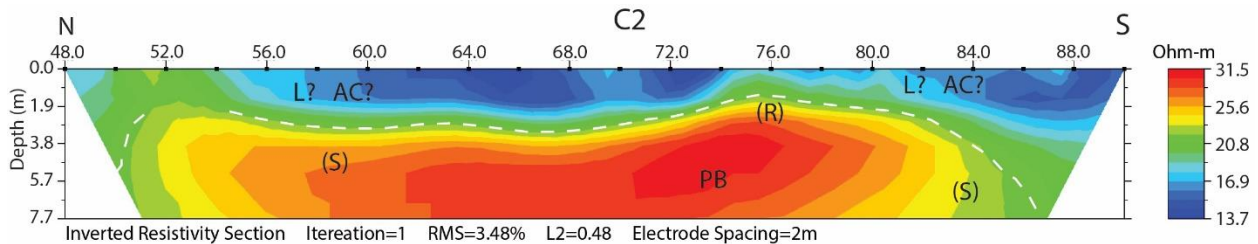


Figure 12. ERT data from Line C2. The second segment from the 286-meter-long ERT profile. L: Levee, AC: Abandoned channel, PB: Pemiscot Bayou Point Bar Deposits, (R): Ridge, (S): Swale. See Figure 5 for location of profile.

In profile segment C3, the low-resistivity area seen in profile C2 continues to overlie the swale and ridge features of the point bar deposits of the Pemiscot Bayou (Figure 13). A large area with higher resistivity (south of 123 m) occurs to the south of the low-resistivity unit. High-resistivities suggest much coarse-grained sediment, possibly a point bar deposit, that breaks through to the surface and forms a sand blow (between 122 m and 130 m). This sand blow is observed on the satellite image of the site (Figure 5).

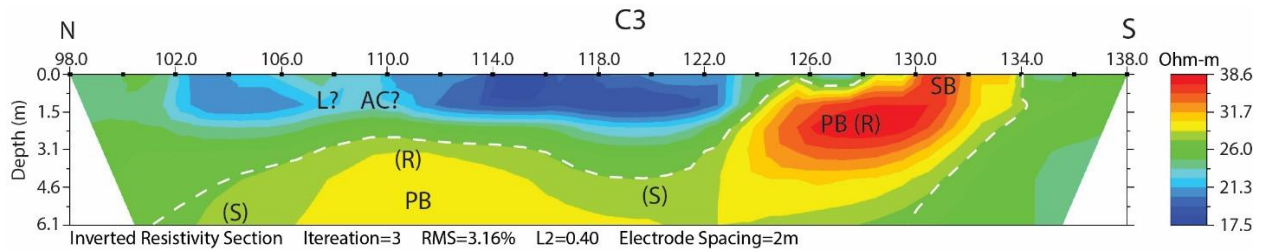


Figure 13. ERT data from Line C3. The third extracted profile from the 286-meter-long ERT profile. L: Levee, AC: Abandoned channel, PB: Pemiscot Bayou Point Bar Deposits, (R): Ridge, (S): Swale, SB: Sand Blow. See Figure 5 for location of profile.

In profile Line C4, a broad, concave-up low-resistivity area underlies a higher resistivity area (Figure 14). The lower unit is interpreted as a fine-grained backswamp deposit. The upper unit, likely composed of course-grained sands and silty sands, may sand blows whose feeder dikes are out of the plane of the cross-section. These areas correspond to light-colored circular deposits seen on the satellite imagery (Figure 5). On the southernmost part of the cross-section, the low-resistivity unit breaches the surface and continues into the north end of profile segment C5 (Figure 15). The variability in resistivity values above ~ 2 m in Line C5 is indicative of interbedded fine and slightly coarse-grained sediment.

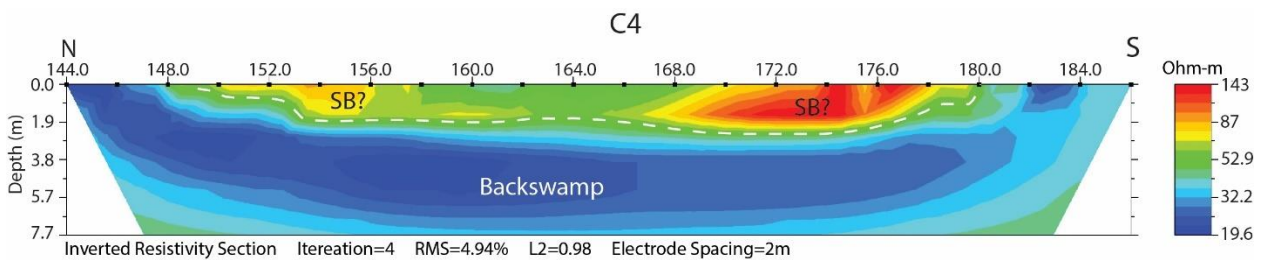


Figure 14. ERT data from Line C4. The low resistivity backswamp deposits are subsided and covered by a high resistivity unit, possibly denoting sand blow deposits. These appear as light-colored circular patches on the satellite imagery in Figure 5. SB: Sand Blow.

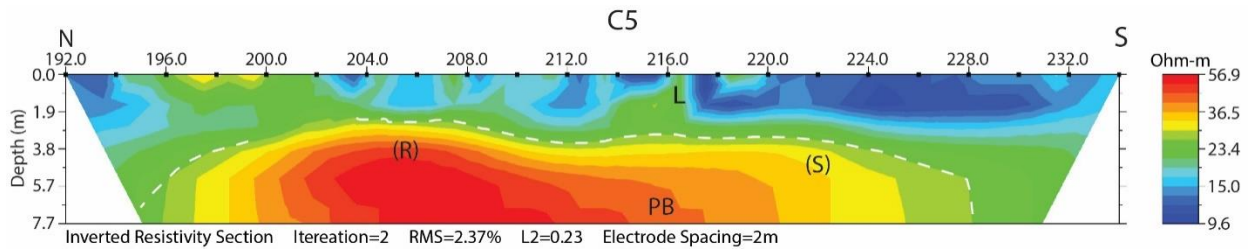


Figure 15. ERT data from Line C5, the fifth extracted profile from the 286-meter-long ERT profile. L: Levee, PB: Pemiscot Bayou Point Bar Deposits, (R): Ridge, (S): Swale, SB: Sand Blow. The combination of low- and moderately high-resistivity areas along the surface are thought to reflect interbedded fine and coarse-grained sediments. See Figure 5 for location of profile.

The final segment of the 286-meter-long-profile, Line C6, is given in Figure 16. The cross-section reveals the subsurface structure below an east-west trending feature seen on the 2010 NAIP satellite imagery towards the current location of the Pemiscot Bayou (Figure 5). This feature is represented with low-resistivity values from 258 m to the south end of the section. This low-resistivity area may represent postulated abandoned channel of the Pemiscot Bayou. The high-resistivity area underlying the low-resistivity unit in the southern end of the profile is interpreted as a point bar deposit of the Pemiscot Bayou. To the north of the low-resistivity unit, a high-resistivity unit extends to the surface. This area is interpreted as a point bar deposit that connects a coarse-grained sand blow, and it aligns on strike with a sand blow observed in the southern ditch exposure.

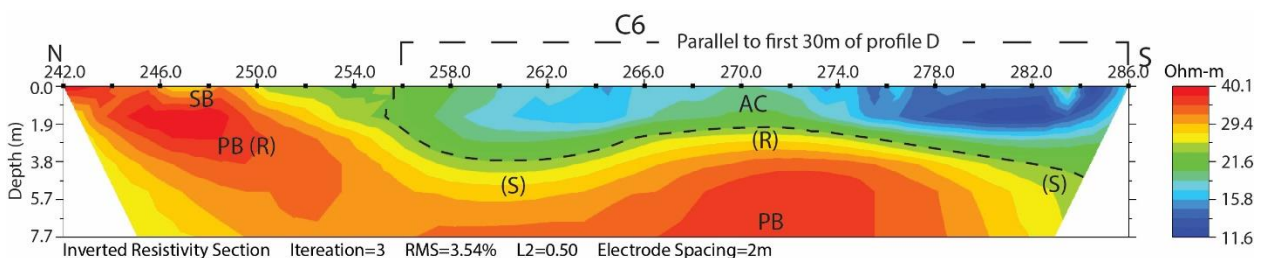


Figure 16. ERT data from Line C6, the final section of the 286-meter-long profile. AC: Abandoned Channel, PB: Pemiscot Bayou Point Bar Deposits, (R): Ridge, (S): Swale, SB: Sand Blow. The sand blow interpreted in the northern end of the profile is on strike with the sand blow observed in the southern ditch exposure. See Figure 5 for location.

The second ERT data set (Line D) acquired in the 2020 field campaign consisted of a 94-m north-south profile (Figure 17), which overlapped the last 30 meters of profile segment C6. This profile was positioned to image the south margin of the postulated abandoned channel as interpreted on Line C6 and on the satellite imagery. The abandoned channel is represented by a low-resistivity area on the north end of the profile to the depth of approximately 7 meters. On the south margin of this low-resistivity unit, a higher resistivity unit breaks through to the surface and is correlated with a sand blow seen in the satellite imagery. The thin, tabular feature between ~33 m and 40 m is interpreted as a sand dike that connects with a sand blow, which extends along the surface to ~ 58 m. The tabular unit appears to be sourced from a deeper, coarse-grained unit interpreted as a point-bar ridge from which entrained sediment-laden water intruded the overlying host sediment to form the sand dike and sand blow. The high-resistivity area at the bottom of the profile (~ 10 m depth and below) is interpreted as a Mississippi River braided stream deposit, inferred based on the models of Guccione *et al.* (1999). The low-resistivity area that lies beneath the sand blow and extends southward to the end of the profile is interpreted as a Mississippi River backswamp deposit, or alternatively, another fine-grained abandoned channel. The higher resistivity region at the surface on the southern end of the profile (~ 73 m – 96 m) is consistent with levee deposits associated with the abandoned channel.

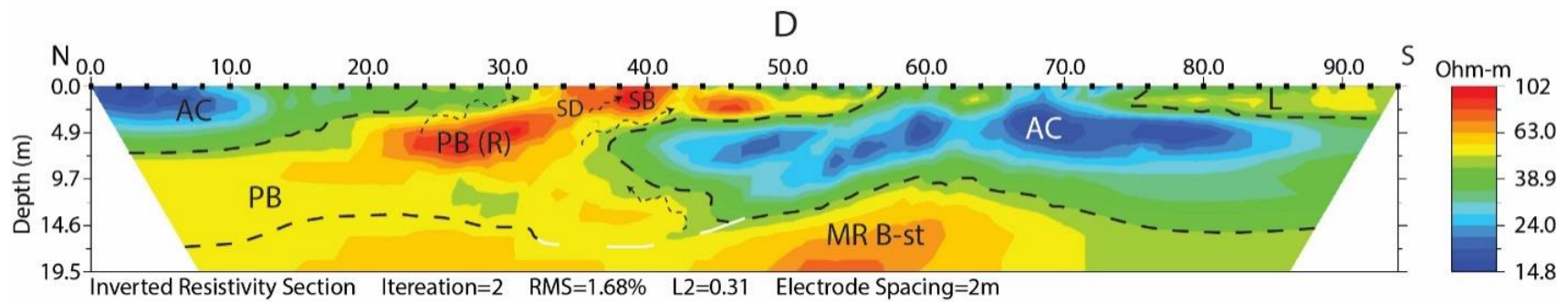


Figure 17. Interpreted ERT profile (Line D) located closest to the current location of the Pemiscot Bayou. AC: Abandoned channel, PB: Pemiscot Bayou Point Bar Deposits, (R): Ridge, (S): Swale, SB: Sand blow, MRBSW: Mississippi River Backswamp Deposits, MR B-st: Mississippi River Braided Stream Deposits, L: Levee deposits. See Figure 5 for location.

Soil Texture Analysis

Auger and surface soil samples were collected during the field visit in October 2020 to assist with the interpretation of satellite imagery and the ERT surveys. Auger samples were taken along the ERT profile lines acquired during the November 2019 field visit (Table 1). Surface soil samples were collected from the Burnham field and three nearby fields that host sand blow deposits. Samples were also acquired from the two ditch exposures. Texture analyses were made using the hydrometer method and depend on the temperature of the environment, the measurement intervals, and the concentration of the chemical dispersion solution. This method leads to some uncertainties in the measurements, and these uncertainties were addressed by repeating the analysis three times to estimate a range of values. The surface soil samples collected may not be fully representative of the site characteristics in terms of sand blow depositions due to the active farming and soil development.

Auger Samples

Soil texture analyses of the auger samples, along with published models of fluvial deposits from the Pemiscot Bayou and Mississippi River, form the basis of the geologic interpretation of the ERT profiles. In this context, hand-augered samples were taken from three different locations at the Burnham site at depths up to one meter. The comparative results are given in Table 1.

The first set of auger samples (first digit = #1) is located on the northern sand blow at 14 m along ERT profile A (Figures 7 and 9). The samples were taken from the depths of 20 cm, 50 cm, and 100 cm (Auger 120, Auger 150, and Auger 1100, respectively, in Table 1). The first sample is from the plow zone and contains the least amount of sand and most amount of carbon

among the three samples. The deeper samples have the texture of sand, which corresponds to higher resistivity values on the ERT profile.

The second auger location (first digit = #5) is at 54 m in the ERT profile (Figures 5 and 9), where an abandoned channel is interpreted. Here, two soil samples were collected at the depths of 30 cm and 80 cm (Auger 530 and Auger 580, respectively, in Table 1). The first sample closest to the surface has silty clay to clay texture. It contains considerably less sand compared to the surface sample of the previous auger location. The texture of the sample from the deeper location has a similar soil texture, but finer materials are abundant in the deeper sample. According to Guccione et al. (1999), abandoned channel fill deposits of the Pemiscot Bayou were associated with silty clay to clay texture, with 46-70% clay content. They suggested that most of the abandoned channel was filled with thin-bedded and fine-grained sediment, with no soil development or bioturbation within the sediment. The results of these samples are consistent with this interpretation.

The final set of auger samples (first digit = #8) are located at 80 m along the ERT profile, where Pemiscot Bayou levee or overbank deposits are interpreted. Both the sample near-surface (40 cm) and the deeper sample (90 cm) have similar textures. The samples indicate a slightly higher percentage of fine-grained sediment than at the 54-m location, which corresponds to the lower resistivity values observed in the ERT profile at the southern end of the line (Figure 9). Consistent with our interpretation of the soil textures and ERT data, Guccione et al. (1999) defined the Pemiscot Bayou natural levee deposits as having silt to clayey silt texture, typically above a point bar sand deposit.

Table 1. Soil texture and carbon content results of the auger samples. The first digit of the sample number refers to the sample location (see Figures 5 and 9). The remaining digits refer to the depth of the sample (cm). Their location relative to the ERT profile is given in Figure 9. Distribution of the sand grains and coordinates of the locations of the samples are given in the appendix section.

	Sample Name	Sand (%)	Silt (%)	Clay (%)	Texture (USDA)	Total Carbon W (%)	Organic Carbon W (%)	Location
Auger 14 m	Auger 120	73 - 77	14 - 18	9 - 11	Sandy loam	0.99	1.21 – 0.75	Plow zone / sand blow
	Auger 150	90 - 94	4 - 8	2 - 4	Sand	0.14 – 0.19	0.13	Sand blow
	Auger 1100	87 - 91	3 - 10	2.5 – 3.5	Sand (close to loamy sand)	0.23	0.27	Sand blow
Auger 54 m	Auger 530	6 - 20	28 - 47	47 - 54	Silty clay to clay	0.87	0.8	Plow zone / abandoned Ch.
	Auger 580	3 - 5	39 - 40	54 - 56	Silty clay to clay	0.53	0.48	Abandoned Channel
Auger 80 m	Auger 840	7 – 10	38 - 41	48 - 54	Silty clay to clay	0.72	1.05	Plow zone / levee or overbank
	Auger 890	3 - 6	47 - 49	46 - 52	Silty clay	0.65	0.95	Levee or overbank

Surface Soil Samples: Burnham Site

The results of the soil texture and carbon content analysis of surface samples from the Burnham site are shown in Table 2. Also included are samples taken from the two ditch exposures at the Burnham site. Eight samples were collected at the Burnham site, five of which were from the northern abandoned channel, and three of which were from the southern abandoned channel closest to the current location of the Pemiscot Bayou. Two of the five samples (BURNS1-D and BURSS1-D) from the north abandoned channel are from the exposures in the cleaned ditch wall. The surface samples from the northern abandoned channel are sandy loam. The sand content is higher compared to the other surface samples from the channel deposit likely because the samples were in close proximity to the liquefaction deposit and could represent ditch spoil. The results of these samples are not believed to accurately reflect the surface soil of the adjacent field but instead are likely a mixture of sediment scraped from the side and bottom of the ditch. The texture of the sample from the southern ditch exposure (BURSS1-D) is sandier and has less carbon content than the sample from the northern ditch exposure (BURNS1-D) and may reflect a greater degree of spoil.

Table 2. Soil texture and carbon content analysis results of the surface samples and the samples from the ditch exposures at the Burnham site. The first three letters of samples names refer the site (BUR for Burnham site). The fourth and fifth letters refer the location (NS: northern sand blow, SS: southern sand blow, AN: north of the abandoned ch., AM: middle of the abandoned ch., AS: south of the abandoned ch.). the sixth place is the sample number. Characters after dash are S for surface samples and D for the samples collected from the ditch exposure. Locations of the samples are shown in satellite image (Figure 5), and distribution of the sand grains and coordinates of the locations of the samples are given in the appendix section.

Sample Name	Sand (%)	Silt (%)	Clay (%)	Texture (USDA)	Total Carbon W (%)	Organic Carbon W (%)	Location
BURNS1-S	68 - 73	15 - 20	12 - 14	Sandy loam	1.27	0.92	Northern sand blow
BURNS2-S	72 - 77	16 - 18	10 - 12	Sandy loam	0.95	0.69	Northern sand blow
BURNS1-D	77 - 78	10 - 12	11 - 12	Sandy loam	0.24	0.43	Northern sand blow
BURSS1-S	70 - 72	18 - 20	10 - 12	Sandy loam	0.75	0.8	Southern sand blow
BURSS1-D	90 - 93	5 - 7	2 - 5	Sand	0.08	N/A	Southern sand blow
BURAN	21 - 25	39 - 43	33 - 38	Silty clay loam to clay loam	1.52	1.56	North of the southmost abandoned ch.
BURAM	18 - 20	53 - 57	23 - 25	Silt loam	1.58	0.96	Middle of the southmost abandoned ch.
BURAS	28 - 29	49 - 54	18 - 23	Silt loam to loam	0.74	0.76	South of the southmost abandoned ch.

Of the remaining three samples, BURAN is taken just north of the abandoned channel closest to the Pemiscot Bayou, BURAM is from within the abandoned channel, and BURAS is from just south of the abandoned channel. The locations of the samples were chosen based on satellite imagery and surface expression. The northern and southern samples have a higher sand content than the sample from the middle of the abandoned channel. According to their location on the imagery and in the ERT profiles, these samples are consistent with sand blow deposits that are adjacent to the margins of the abandoned channel deposit. The silt content of the northern sample is higher than that of the southern sample. Guccione *et al.* (1999) defined the texture of the Pemiscot Bayou levee deposits to be siltier than the Mississippi River backswamp deposits. For this reason, the northern sample is associated with a sand blow and levee deposit, and the southern sample is interpreted as a combination of a sand blow and backswamp deposit. However, a similar correlation in carbon content analysis cannot be observed.

Surface Soil Samples: Bugg 40 and Dillahunty Sites

Two surface samples were collected from the Bugg 40 site (Figure 18A), one from a large liquefaction deposit (BUGS1) and the other from host sediments (BUGR1) (Table 3). The sample locations were chosen to allow a textual comparison between the two types of deposits at the site. Although both samples have a similar texture, the sample from the liquefaction has more sand and less carbon content compared to the sample from the host sediment.

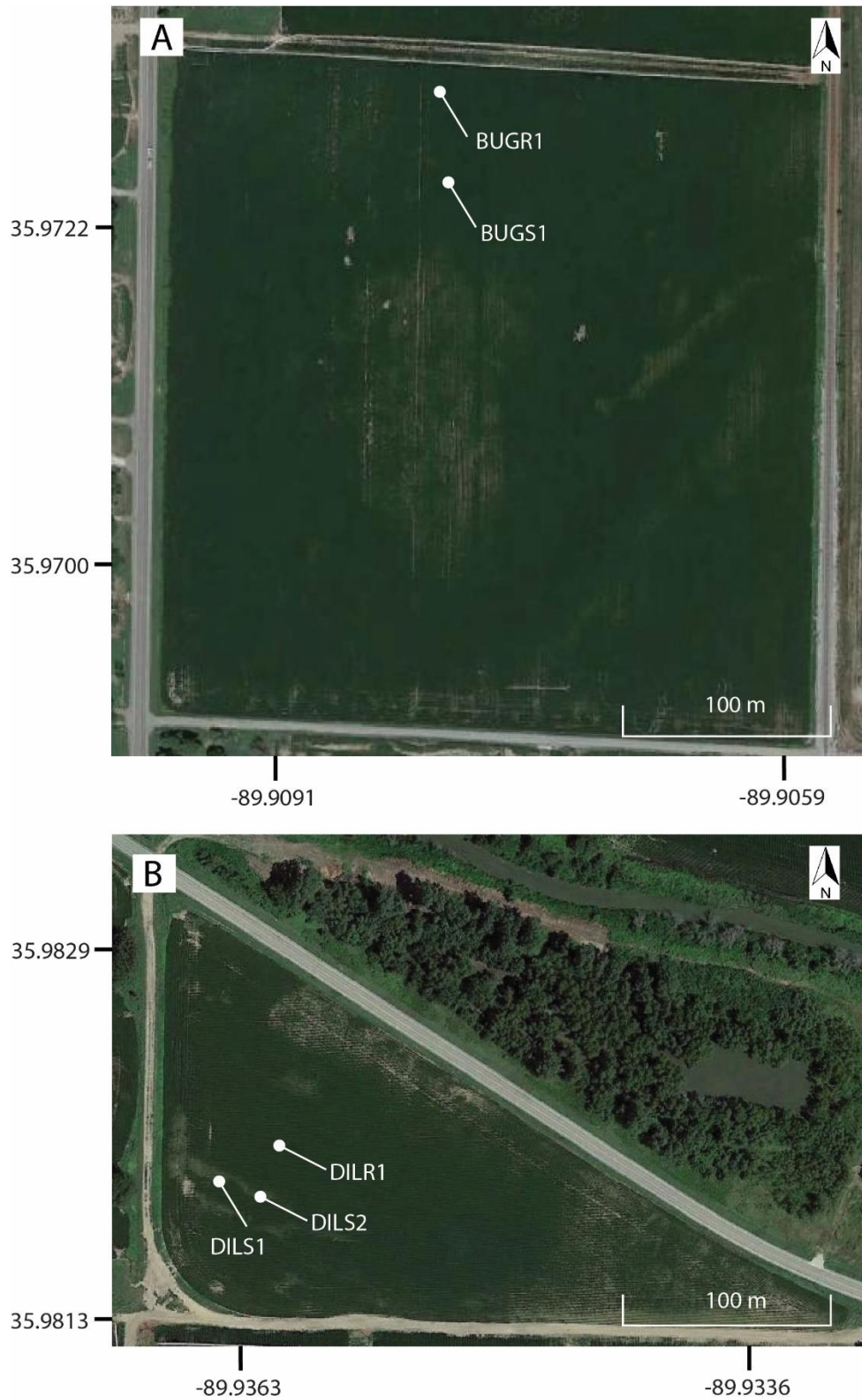


Figure 18. Google Earth image of the Bugg 40 (A) and Dillahunty (B) sites (August 14, 2019), showing the locations of surface soil samples collected on both sand blow and host sediments.

Table 3. Soil texture and carbon content analysis results of the surface samples from the Bugg 40 site. The first three letters of samples names refer the site (BUG for Bugg 40 site). The fourth letter refers the location (S: sand blow, R: host sediment). The fifth place is the sample number. Locations of the samples are shown in satellite image (Figure 18A), and distribution of the sand grains and coordinates of the locations of the samples are given in the appendix section.

Sample Name	Sand (%)	Silt (%)	Clay (%)	Texture (USDA)	Total Carbon W (%)	Organic Carbon W (%)	Location
BUGS1	39 - 41	42 - 47	13 - 18	Loam	0.93	0.93	Sand blow
BUGR1	30 - 33	44 - 48	20 - 24	Loam	1.23	1.13 – 0.87	Host sediment

Table 4. Soil texture and carbon content analysis results of the surface samples from the Dillahunty site. The first three letters of samples names refer the site (DIL for Dillahunty site). The fourth letter refers the location (S: sand blow, R: host sediment). The fifth place is the sample number. Locations of the samples are shown in satellite image (Figure 18B), and distribution of the sand grains and coordinates of the locations of the samples are given in the appendix section.

Sample Name	Sand (%)	Silt (%)	Clay (%)	Texture (USDA)	Total Carbon W (%)	Organic Carbon W (%)	Location
DILS1	33 - 37	47 - 51	14 - 18	Silt loam to loam	0.92 – 0.94	1.26	Sand blow
DILS2	35 - 38	46 - 50	17 - 20	Loam	0.77 – 0.79	0.85	Sand blow
DILR1	37 - 41	46 - 50	11 - 15	Silt loam to loam	0.87 – 0.89	0.61 – 0.64	Host sediment

Three surface samples were collected from the Dillahunty site (Figure 18B), two from the liquefaction features (DILS1 and DILS2) (Table 4), and the other from a random location representing host sediments (DILR1). The results of the texture analysis indicate that the samples are similar to one another. The texture of the DILS1 and DILR1 is silt loam to loam, while DILS2 has only the loam texture. Unlike the texture results of the samples from the Bugg 40 site, surface samples of the sand blow at the Dillahunty site appeared to have similar sand content than the host sediment sample from the site. Because the Dillahunty site is located next to the current location of the Pemiscot Bayou, the field may be under the influence of the channel deposits of the Pemiscot Bayou. Schneider and Mayne (1999) studied a location approximately 20-30 meters away from the surface samples collected for this study from the Dillahunty site. Their borehole results show mostly sand interbedded with a few clayey silt layers. These findings suggest that the textures and carbon content of samples from the Dillahunty site can be explained by sandy host deposits that show little distinction from the sand blow deposits.

Timing of the Events

The two distinct sand blow depositional units observed in the ditch exposures at the Burnham site suggest that they could have resulted from two phases within an earthquake sequence or two different earthquakes of different ages (Figures 7 and 8). Although examination of these units revealed a silty layer separating the two sand blow units in the southern ditch exposure, there was no soil development observed in this silty layer. In the northern exposure, there is no silty layer separating the two sand blow units. Weathering characteristics, the number of depositional units, and the absence of heavy bioturbation and soil development in each sand horizon suggest that the sand blows formed during the same earthquake sequence, in which two events occurred one after the other.

To understand the timing of the earthquakes responsible for the liquefaction deposits, five organic samples were collected for radiocarbon dating from the soil buried by the sand blow. Plant material taken from the north ditch exposure at the contact surface of the buried soil and sand blow, approximately 60-65 cm below the surface (Figure 7B), provided a maximum constraining age, which indicated that the liquefaction features formed some time later. The result of radiocarbon age determination was provided with an accuracy rate of 95.4 percent, 65.6 percent of which corresponds to the calibrated age range of 1445-1340 yr B.P, and 29.8 to the calibrated age range of 1522-1452 yr B.P. In addition, sand blows at the southern exposure formed soil lamellae, a process that likely took hundreds to thousands of years and indicates that the sand blows are prehistoric in age (Tuttle, 2001; Tuttle *et al.*, 2019). Based on these observations, the earthquake that caused the liquefaction is best aligned with the A.D. 900 +/- 150 yr New Madrid earthquake sequence. However, other interpretations are possible and additional dating is needed to constrain better the age of the features.

DISCUSSION

The ERT surveys conducted at the Burnham site were useful in capturing the liquefaction features, their relations to the host sediments, and the fluvial environment associated with the Pemiscot Bayou. The ERT surveys measure apparent resistivity in the field. An inversion process converts the data to reflect the true resistivity distribution in the subsurface. The accuracy of the inversion is tested by assuming the true resistivity distribution is correct and predicting the apparent resistivity through forward modeling. An estimate of accuracy is obtained from a comparison of the predicted values with the observed values. The accuracy is reflected by the RMS error and L2 norm (Advanced Geosciences, 2009). The lower RMS and L2 values indicate more accurate results.

The ERT results are principally controlled by moisture, fluid type, grain size, and void size as a function of grain size (Archie, 1942). Compared to host sediments that are mainly silty clay to clay, sand blows generally exhibit higher resistivity values because of their coarser grain sizes and considerably lower gravimetric water content. Although this relationship was generally well supported by the ERT data at the Burnham site, the very near-surface sediment properties at some locations along the profile did not always agree with the subsurface values.

The interpretation of the ERT results is in accordance with the sedimentological models of the Pemiscot Bayou and nearby areas as developed by Kendall (1997) and Guccione *et al.* (1999). The study site is composed of Holocene meander-belt deposits from the Pemiscot Bayou and Late Pleistocene braided stream and backswamp deposits of the Mississippi River (Saucier, 1994; Tuttle *et al.*, 2019). Comparison of the Line A and B profiles (Figures 9 and 10) in the context of these models supports the interpretation that the dark brown east-west-trending

lineaments seen in the satellite data of the Burnham site (Figure 5) likely represent abandoned channels of the Pemiscot Bayou.

The C1 ERT profile, which is a segment of the 286-meter-long profile, overlaps with the Line A and B profiles and contains a high-resistivity area interpreted as a point bar deposit and a low-resistivity area interpreted as a possible levee or overbank deposit. Although the low-resistivity areas on the C2 and C3 profiles were initially considered to be levee or overbank deposits, the satellite imagery shows this region of the profile coincident with the west-northwest-oriented lineament that is most likely a smaller channel fill deposit (Figure 5). This conclusion is supported by Kendall (1997) and Guccione *et al.* (1999), who assert that the Pemiscot Bayou shows several generations of channel-fill deposits. South of the interpreted abandoned channel in Lines C2 and C3, the satellite imagery indicates two possible sand blows that are oriented north-northwest. These features appear to continue and become more prominent on the west side of the north-south-oriented ditch (Figure 5).

In general, the ERT profiles show low-resistivity units overlying higher resistivity units. However, this trend is not the case for the C4 profile. Here, a high-resistivity area buries a wedge-shaped low-resistivity unit. There are several possible explanations. First, a faulty electrode at 146 m along the line may have affected the results, at least in the near surface. Secondly, the C4 profile shows similarity with the upper portion of the Line B profile from 0 m to 20 m, where the northern sand blow overlies a low-resistivity unit interpreted as a backswamp deposit. The area below the C4 profile might represent an island of Pleistocene braided stream deposits, which are overlain by a backswamp deposit that was not reworked by the Pemiscot Bayou. Although the area of high resistivity near the top of the profile requires more research, it

could be interpreted as a sand blow deposit in which the feeder dike exists outside of the plane of the cross-section.

The C6 and D profiles reveal another near-surface area of low-resistivities interpreted as a second abandoned channel, which is also seen as a dark-colored east-west-oriented lineament in the satellite image. The channel width in Line C6 and Line D is approximately 35 meters, similar to the channel revealed by the Line A and B profiles; however, the depth of the abandoned channel interpreted in Line C6 and Line D is approximately half. This observation can be explained as a loss in the energy of water in the channel, which led to less sediment being deposited or to channel migration. The available energy of the flow may have been reduced by the development of a cut-off of the Mississippi River meander bend, along which the distributary node was located, and consequently, the discharge into the distributary channel may have been reduced (Guccione *et al.*, 1999). Although the low-resistivity area towards the south of Line D was identified as a backswamp deposit, it could be another abandoned channel-fill deposit that was later buried by a high-resistivity unit at the southernmost end of the profile (Figure 17).

Factors Controlling Liquefaction at the Burnham Site

Soil composition, especially particle size distribution, shape, and cohesion, are factors influencing liquefaction susceptibility; sand grains that are evenly distributed and have a rounded grain shape are more susceptible to liquefaction than fine-grained clayey units (Kramer and Elgamal, 2002). As porous, water-saturated layers are shaken, excess fluid pressure can increase if confining units are present that restrict fluid pressure dissipation (National Research Council, 1985). Fluvial deposits consisting of fine- to medium-grained saturated sands are commonly associated with high liquefaction susceptibility (e.g., Seed and Idriss, 1982; Tuttle and Barstow, 1996; Tuttle, 2001). These deposits, interbedded with fine-grained units, form a structure that

facilitates the liquefaction process during cyclic loading from earthquake strong ground motions. Results from the Burnham site suggest a subsurface architecture of interbedded fluvial deposits that are consistent with the required conditions for earthquake-induced liquefaction

Examination of the satellite imagery and the ERT data suggest that the sand blows are arranged along and subparallel to the margins of the abandoned channels (Figures 5, 9, and 10). In lines A and B, the subsurface structure below ~8 m depth to the north of the abandoned channel hosts high-resistivity, coarse-grained deposits that would have high permeability and liquefaction susceptibility (Figures 9 and 10). This area is overlain by low-resistivity, fine-grained backswamp and levee deposits that would be associated with low permeability and could serve as a confining unit that allows fluid pressures to build up during earthquake-generated strong ground motion (Tuttle and Barstow, 1996; Frost, 2001; Tuttle, 2001). South of the sand blow seen in Lines A and B and the satellite imagery (Figure 5), the point bar deposit interpreted for the area below ~ 3 m depth would be associated with moderately high permeability. This area is overlain by a levee or overbank deposit, which could also serve as a confining unit. In both cross-sections, a tabular high-resistivity area breaks through the lower resistivity areas on either side of the abandoned channel. These breaks likely represent the pathways for overpressured liquefied sediment to escape to the surface. Examination of the sand dikes in the ditch exposures revealed a subsurface arrangement that is similar to that seen in the ERT profiles but that offers more detail. The dip direction of the sand dikes observed in the two logged ditch exposures are towards the abandoned channel (Figures 7 and 8). This orientation suggests that the fine-grained sediments in the channel acted as an impermeable barrier, forcing the flow of liquefied sediments along its contact with the adjacent, more permeable units. The liquefaction deposits in the ditch exposures suggest the vigorous upward flow of water and entrained sediment formed the sand

dikes and sand blows from a source unit below. Fallback clasts in the vent area and a clast-rich zone in the sand blow reflect the intense pressure and the consequential forceful venting of the liquefied sediment.

Dobry and Liu (1992), Fiegel and Kutter (1992, 1994) proposed models examining the effect of an impermeable layer overlying a permeable layer on earthquake-induced liquefaction features by simulating an earthquake with a centrifuge containing sand and impermeable silt layers. They proposed that the impermeable overlying layer prevents the pore water from escaping and a water layer is formed along the gap between the permeable and impermeable layers. If a crack or a bulge occurs in an impermeable layer, the mixture of eroded sand and water is carried to the surface as a result of excess pressure. These models support the model proposed at the Burnham site in which the sand blows found at the margins of the abandoned channels imaged in Lines C3, C6 and D were guided to the surface along the contact of the less permeable channel deposits that occur alongside and above the coarse-grained point bar and braided stream deposits that served as source units for the sand dikes and sand blows.

Although the interpretation of the ERT data is helped by the satellite images of the Burnham site, the data also suggest some high-resistivity areas in the subsurface that may represent pathways for liquefied sediment that failed to reach the surface and form sand blows. Fiegel and Kutter (1992) proposed that liquefied sand can create a bulge on a thin impermeable layer and can weaken the layer. The weakened layer forms cracks and fractures, creating a pathway for liquefaction that does not reach the surface. The area near 72 m in Line C2 and 270 m in Line C6 profile could represent bulges that formed during the liquefaction process, even though the liquefied sand never made it to the surface (at least along the plane of the cross-

section). In contrast, the area with high resistivity around 52 m in line C2 profile is probably a point bar ridge that served as the source unit for the sand blow and related dikes.

Finally, while two abandoned channels at the Burnham site (imaged in ERT Lines A, B, C6, and D) have a roughly east-west orientation, the abandoned channels imaged in Lines C2 and C3 have a west-northwest orientation, suggesting that they may represent different generations of deposits in the stream evolution. Further work needs to be done to determine the evolution of the Pemiscot Bayou and its former channels at the site.

CONCLUSION

ERT surveys in combination with satellite imagery, soil sampling, and detailed logging of exposed liquefaction features at the Burnham site in northeastern Arkansas provide insight into the interplay of sedimentary architecture on the liquefaction process as well as the timing of earthquakes responsible for liquefaction features found in ditch exposures at the site. The distribution of fluvial sediments at the site suggests that the subsurface arrangement of deposits with differing physical properties and associated permeabilities contribute to the fluidization of sedimentary deposits and the consequential location of liquefaction features. Fine-grained sediments associated with levee and overbank deposits create low-permeability areas that allow fluid pressures to build up in more permeable layers below during strong ground shaking from earthquake-generated motions. At this site, liquefied source sands appear to follow pathways along the margins of an abandoned channel fill deposit, forming sand dikes that connect to vented sand (sand blows) on the surface. Inclined contacts between fine-grained abandoned channel deposits and coarse-grained braided stream and point bar deposits, as imaged in the ERT data and observed in the ditch exposures, served as mechanical and geometrical boundaries guiding the flow of the escaping fluidized sand and influencing the emplacement of sand dikes and formation of sand blows (Tuttle and Barstow, 1996). The ERT profiles captured two, and possibly three, abandoned channels and revealed at least two sand blows along the margins of channels.

Radiocarbon analysis and soil development characteristics of the sand blows observed in the ditch exposures suggest that the liquefaction features likely formed during the A.D. 900 +/- 150 yr. New Madrid event. This date is in agreement with an earthquake chronology established

for the NMSZ and consistent with other deposits discovered in the area. (Tuttle *et al.*, 1999, 2002, 2005, 2019). In addition, the presence of two depositional sand blow units in both exposures suggests that the exposures may record two earthquakes within a single series.

REFERENCES

- Advanced Geosciences, I. (AGI) (2009). EarthImager 2D, no. 512, 139.
- Archie, G. E. (1942). The electrical resistivity log as an aid in determining some reservoir characteristics, *Trans. AIME* **146**, no. 01, 54–62.
- Bockheim, J. G. (2014). Soils with Lamellae, in *Soil Geography of the USA: A Diagnostic-Horizon Approach*, Springer International Publishing, Cham, 283–300, doi: 10.1007/978-3-319-06668-4_24.
- Braile, L. W., W. J. Hinze, G. R. Keller, E. G. Lidiak, and J. L. Sexton (1986). Tectonic development of the New Madrid rift complex, Mississippi embayment, North America, *Tectonophysics* **131**, no. 1–2, 1–21.
- Cox, R. T., and R. B. Van Arsdale (2002). The Mississippi Embayment, North America: a first order continental structure generated by the Cretaceous superplume mantle event.
- Cramer, C. H. (2001). A seismic hazard uncertainty analysis for the New Madrid seismic zone, *Eng. Geol.* **62**, no. 1–3, 251–266, doi: 10.1016/S0013-7952(01)00064-3.
- Cushing, E. M., E. H. Boswell, and R. L. Hosman (1964). General geology of the Mississippi embayment.
- Dobry, R., and L. Liu (1992). Centrifuge modeling of soil liquefaction, in *Proc., 10th World Conf. on Earthquake Engineering*, International Association for Earthquake Engineering (IAEE) Madrid, Spain, 6801–6809.
- Elnashai, A. S., L. J. Cleveland, T. Jefferson, and J. Harrald (2009). Impact of New Madrid

seismic zone earthquakes on the Central USA, Vol. 1 and 2.

Ervin, C. P., and L. D. McGinnis (1975). Reelfoot rift: Reactivated precursor to the Mississippi embayment, *Bull. Geol. Soc. Am.* **86**, no. 9, 1287–1295, doi: 10.1130/0016-7606(1975)86<1287:RRRPTT>2.0.CO;2.

Fiegel, G. L., and B. L. Kutter (1994). Liquefaction mechanism for layered soils, *J. Geotech. Eng.* **120**, no. 4, 737–755.

Fiegel, G. L., and B. L. Kutter (1992). The mechanism of liquefaction in layered soils, CALIFORNIA UNIV DAVIS.

Frost, J. D. (2001). Paleoseismology and paleoliquefaction, Georgia Institute of Technology.

Gee, G. W., and D. Or (2002). 2.4 Particle-Size Analysis, SSSA Book Series, 255–293, doi: <https://doi.org/10.2136/sssabookser5.4.c12>.

Giona Bucci, M., P. Villamor, P. Almond, M. Tuttle, M. Stringer, W. Ries, C. Smith, M. Hodge, and M. Watson (2018). Associations between sediment architecture and liquefaction susceptibility in fluvial settings: The 2010–2011 Canterbury Earthquake Sequence, New Zealand, *Eng. Geol.* **237**, no. November 2017, 181–197, doi: 10.1016/j.enggeo.2018.01.013.

Gold, R. D., C. B. DuRoss, J. E. Delano, R. W. Jibson, R. W. Briggs, S. A. Mahan, R. A. Williams, and D. R. Corbett (2019). Four major Holocene earthquakes on the Reelfoot fault recorded by sackungen in the New Madrid seismic zone, USA, *J. Geophys. Res. Solid Earth* **124**, no. 3, 3105–3126.

Gomberg, J., and M. Ellis (1994). Topography and tectonics of the central New Madrid seismic zone: Results of numerical experiments using a three-dimensional boundary element

- program, *J. Geophys. Res. Solid Earth* **99**, no. B10, 20299–20310.
- Guccione, M. J., M. F. Burford, and J. D. Kendall (1999). Pemiscot Bayou, a Large Distributary of the Mississippi River and a Possible Failed Avulsion, Wiley Online Books, 211–220, doi: <https://doi.org/10.1002/9781444304213.ch16>.
- Guccione, M. J., R. H. Lafferty III, and L. S. Cummings (1988). Environmental constraints of human settlement in an evolving Holocene alluvial system, the Lower Mississippi Valley, *Geoarchaeology* **3**, no. 1, 65–84.
- Harris, D., W. R. Horwáth, and C. van Kessel (2001). Acid fumigation of soils to remove carbonates prior to total organic carbon or CARBON-13 isotopic analysis, *Soil Sci. Soc. Am. J.* **65**, no. 6, 1853–1856, doi: 10.2136/sssaj2001.1853.
- Hildenbrand, T. G., M. F. Kane, and W. S. J. Stauder (1977). Magnetic and gravity anomalies in the northern Mississippi Embayment and their spacial relation to seismicity.
- Johnston, A. C., and S. J. Nava (1985). Recurrence rates and probability estimates for the New Madrid Seismic Zone, *J. Geophys. Res.* **90**, no. B8, 6737, doi: 10.1029/jb090ib08p06737.
- Kelson, K. I., G. D. Simpson, R. B. VanArsdale, C. C. Haraden, and W. R. Lettis (1996). Multiple late Holocene earthquakes along the Reelfoot fault, central New Madrid seismic zone, *J. Geophys. Res. Solid Earth* **101**, no. B3, 6151–6170.
- Kendall, J. D. (1997). Sedimentation and seismic modification of Pemiscot Bayou, Yarbrow, Arkansas, University of Arkansas, Fayetteville, AR.
- Kramer, S. L., and A. W. M. Elgamal (2002). *Modeling Soil Liquefaction Hazards for Performance-based Earthquake Engineering*, Pacific Earthquake Engineering Research

Center, PEER report.

Mooney, W. D., M. C. Andrews, A. Ginzburg, D. A. Peters, and R. M. Hamilton (1983). Crustal structure of the northern Mississippi embayment and a comparison with other continental rift zones, *Tectonophysics* **94**, no. 1–4, 327–348.

National Research Council (1985). Liquefaction of soils during earthquakes, *Comm. Earthq. Eng.*

Obermeier, S. F. (1989). The New Madrid earthquakes: an engineering–geologic interpretation of relict liquefaction features, *US Geol. Surv. Prof. Pap.* **1336 B**, doi: 10.3133/pp1336b.

Owen, G. (1987). Deformation processes in unconsolidated sands, *Geol. Soc. Spec. Publ.* **29**, no. 29, 11–24, doi: 10.1144/GSL.SP.1987.029.01.02.

Pollitz, F. F., and W. D. Mooney (2014). Seismic structure of the Central US crust and shallow upper mantle: Uniqueness of the Reelfoot Rift, *Earth Planet. Sci. Lett.* **402**, 157–166.

Price, A. C., E. W. Woolery, R. C. Counts, R. B. Van Arsdale, D. Larsen, S. A. Mahan, and E. G. Beck (2019). Quaternary Displacement on the Joiner Ridge Fault, Eastern Arkansas, *Seismol. Res. Lett.* **90**, no. 6, 2250–2261.

Royall, P. D., P. A. Delcourt, and H. R. Delcourt (1991). Late Quaternary paleoecology and paleoenvironments of the central Mississippi alluvial valley, *Geol. Soc. Am. Bull.* **103**, no. 2, 157–170.

Russ, D. P. (1979). Late Holocene faulting and earthquake recurrence in the Reelfoot Lake area, northwestern Tennessee, *Geol. Soc. Am. Bull.* **90**, no. 11, 1013–1018.

Saucier, R. T. (1977). *Effects of the New Madrid earthquake series in the Mississippi alluvial*

- valley, US Waterways Experiment Station.
- Saucier, R. T. (1964). *Geological investigation of the St. Francis basin*, US Army Engineer Waterways Experiment Station, Corps of Engineers.
- Saucier, R. T. (1994). Geomorphology and Quaternary Geologic History of the Lower Mississippi Valley, *US Army Corps Eng. I*, 1–414.
- Saucier, R. T. (1974). *Quaternary Geology of the Lower Mississippi Valley*, Arkansas Archeological Survey, Arkansas Archeological Survey research series.
- Schneider, J. A., and P. W. Mayne (1999). Soil liquefaction response in mid-America evaluated by seismic piezocone tests, *Mid-America Earthq. Cent. CD Release 00-03*.
- Schwalb, H. R. (1969). Paleozoic geology of the Jackson Purchase region, *Kentucky Kentucky Geol. Surv. Rep. Investig. 10*, 40.
- Seed, B. (1979). Soil liquefaction and cyclic mobility evaluation for level ground during earthquakes, *J. Geotech. geoenvironmental Eng.* **105**, no. ASCE 14380.
- Seed, H. B., and I. M. Idriss (1982). *Ground Motions and Soil Liquefaction During Earthquakes*, Earthquake Engineering Research Institute, Engineering monographs on earthquake criteria, structural design, and strong motion records.
- Smalley, R., M. A. Ellis, J. Paul, and R. B. Van Arsdale (2005). Space geodetic evidence for rapid strain rates in the New Madrid seismic zone of central USA, *Nature* **435**, no. 7045, 1088–1090.
- Smith, F., and R. Saucier (1971). *Geological Investigation of the Western Lowlands Area, Lower Mississippi Valley*.

- Thomas, W. A. (2006). Tectonic inheritance at a continental margin, *GSA today* **16**, no. 2, 4–11.
- Thompson Jobe, J. A., R. D. Gold, R. W. Briggs, R. A. Williams, W. J. Stephenson, J. E. Delano, A. Shah, and B. Minsley (2020). Evidence for late Quaternary deformation along Crowleys Ridge, New Madrid seismic zone, *Tectonics* **39**, no. 4, e2019TC005746.
- Tuttle, M. P. (2010). Search for and study of sand blows at distant sites resulting from prehistoric and historic New Madrid earthquakes: Collaborative Research. M. Tuttle & Associates and Central Region Hazards Team, *US Geol. Surv. Final Tech. Rep.*
- Tuttle, M. P. (2001). The use of liquefaction features in paleoseismology: Lessons learned in the New Madrid seismic zone, Central United States, *J. Seismol.* **5**, no. 3, 361–380, doi: 10.1023/A:1011423525258.
- Tuttle, M., and N. Barstow (1996). Liquefaction-related ground failure: A case study in the New Madrid seismic zone, central United States, *Bull. Seismol. Soc. Am.* **86**, no. 3, 636–645.
- Tuttle, M. P., J. Collier, L. W. Wolf, and R. H. Lafferty (1999). New evidence for a large earthquake in the New Madrid seismic zone between A.D. 1400 and 1670, *Geology* **27**, no. 9, 771–774, doi: 10.1130/0091-7613(1999)027<0771:NEFALE>2.3.CO;2.
- Tuttle, M. P., R. Hartleb, L. Wolf, and P. W. Mayne (2019). Paleoliquefaction studies and the evaluation of seismic hazard, *Geosci.* **9**, no. 7, 1–61, doi: 10.3390/geosciences9070311.
- Tuttle, M. P., and E. S. Schweig (1996). Recognizing and dating prehistoric liquefaction features: Lessons learned in the New Madrid seismic zone, central United States, *J. Geophys. Res. B Solid Earth* **101**, no. 3, 6171–6178, doi: 10.1029/95jb02894.
- Tuttle, M. P., E. S. Schweig, J. Campbell, P. M. Thomas, J. D. Sims, and R. H. Lafferty (2005).

- Evidence for New Madrid earthquakes in AD 300 and 2350 BC, *Seismol. Res. Lett.* **76**, no. 4, 489–501.
- Tuttle, M. P., E. S. Schweig, J. D. Sims, R. H. Lafferty, L. W. Wolf, and M. L. Haynes (2002). The earthquake potential of the New Madrid seismic zone, *Bull. Seismol. Soc. Am.* **92**, no. 6, 2080–2089, doi: 10.1785/0120010227.
- Tuttle, M. P., L. W. Wolf, M. E. Starr, P. Villamor, R. H. Lafferty, K. Hess, J. E. Morrow, R. J. Scott, S. L. Forman, K. Tucker, *et al.* (2019). Evidence for large New Madrid earthquakes about A.D. 0 and 1050 B.C., central United States, *Seismol. Res. Lett.* **90**, no. 3, 1393–1406, doi: 10.1785/0220180371.
- Van Arsdale, R. B. (2009). *Adventures through deep time: The central Mississippi River Valley and its earthquakes*, Geological Society of America.
- USDA (2010). National Agriculture Imagery Program (NAIP): <<https://earthexplorer.usgs.gov/>> (accessed date 1/20/2021).
- USGS (2021). Search Earthquake Catalog: <<https://earthquake.usgs.gov/earthquakes/search/>> (accessed date 3/26/2021).
- Ward, S. H. (1990). 6. Resistivity and Induced Polarization Methods, in *Geotechnical and Environmental Geophysics: Volume I, Review and Tutorial*, Society of Exploration Geophysicists, Investigations in Geophysics, 147–190, doi: doi:10.1190/1.9781560802785.ch6.
- Wolf, L. W., J. Collier, M. Tuttle, and P. Bodin (1998). Geophysical reconnaissance of earthquake-induced liquefaction features in the New Madrid seismic zone, *J. Appl.*

Geophys. **39**, no. 3, 121–129, doi: 10.1016/S0926-9851(98)00016-0.

Wolf, L. W., M. P. Tuttle, S. Browning, and S. Park (2006). Geophysical surveys of earthquake-induced liquefaction deposits in the New Madrid seismic zone, *Geophysics* **71**, no. 6, doi: 10.1190/1.2353801.

APPENDIX A

Appendix A contains gravimetric water contents and coordinates of the auger samples from the Burnham site and surface soil samples from the Burnham, the Dillahunty and the Bugg 40 sites. Also, this section has the coordinates of the ERT profiles from the Burnham site.

Table A-1. Gravimetric water content and coordinates of the auger samples.

Sample Name	Gravimetric water content (g/g)	Coordinates	
		Longitude	Latitude
Auger 120	0.017293998	-89.92779265	35.98616369
Auger 150	0.010090817	-89.92779265	35.98616369
Auger 1100	0.012762953	-89.92779265	35.98616369
Auger 530	0.075662093	-89.92782213	35.9858258
Auger 580	0.084507042	-89.92782213	35.9858258
Auger 840	0.096280088	-89.92785236	35.98559007
Auger 890	0.080547591	-89.92785236	35.98559007

Table A-2. Gravimetric water content and coordinates of the surface and ditch exposure samples of the Burnham site.

Sample Name	Gravimetric water content (g/g)	Coordinates	
		Longitude	Latitude
BURNS1-S	0.021406728	-89.92794583	35.98619894
BURNS2-S	0.009045226	-89.92795151	35.98617851
BURNS1-D	0.012133468	-89.9279659	35.98617361
BURSS1-S	0.016243655	-89.92796344	35.9856924
BURSS1-D	0.002004008	-89.92797949	35.98569829
BURAN	0.053571429	-89.92796433	35.98357604
BURAM	0.042708333	-89.92789984	35.98318047
BURAS	0.035151849	-89.92794838	35.98276403

Table A-3. Gravimetric water content and coordinates of the surface and ditch exposure samples of the Bugg 40 site.

Sample Name	Gravimetric water content (g/g)	Coordinates	
		Longitude	Latitude
BUGS1	0.030927835	-89.90802971	35.97248945
BUGR1	0.038421599	-89.9081179	35.97302989

Table A-4. Gravimetric water content and coordinates of the surface and ditch exposure samples of the Dillhanty site.

Sample Name	Gravimetric water content (g/g)	Coordinates	
		Longitude	Latitude
DILS1	0.023493361	-89.9365329	35.98194245
DILS2	0.026694045	-89.93644327	35.9819105
DILR1	0.010090817	-89.93635053	35.98211804

Table A-5. Distance and the coordinates of the ERT profiles.

ERT Profile Name	Distance		Coordinates	
			Longitude	Latitude
Line A	Start	0 m	-89.927786	35.986314
	Finish	94 m	-89.927821	35.984863
Line B	Start	0 m	-89.927677	35.986318
	Finish	94 m	-89.927659	35.985473
Line C1	Start	0 m	-89.927911	35.985646
	Finish	42 m	-89.927924	35.985269
Line C2	Start	48 m	-89.927926	35.985212
	Finish	90 m	-89.927939	35.984832
Line C3	Start	98 m	-89.927941	35.984765
	Finish	138 m	-89.927954	35.984404
Line C4	Start	144 m	-89.927956	35.984349
	Finish	186 m	-89.927969	35.983958
Line C5	Start	192 m	-89.927971	35.983912
	Finish	232 m	-89.927983	35.983551
Line C6	Start	242 m	-89.927912	35.983470
	Finish	286 m	-89.927922	35.983073
Line D	Start	0 m	-89.927862	35.983349
	Finish	94 m	-89.927892	35.982502

APPENDIX B

Appendix B contains particle size distribution graphs of the sand grains of the auger samples collected from the Burnham site and surface soil samples collected from the Burnham, the Dillahunty and the Bugg 40 sites.

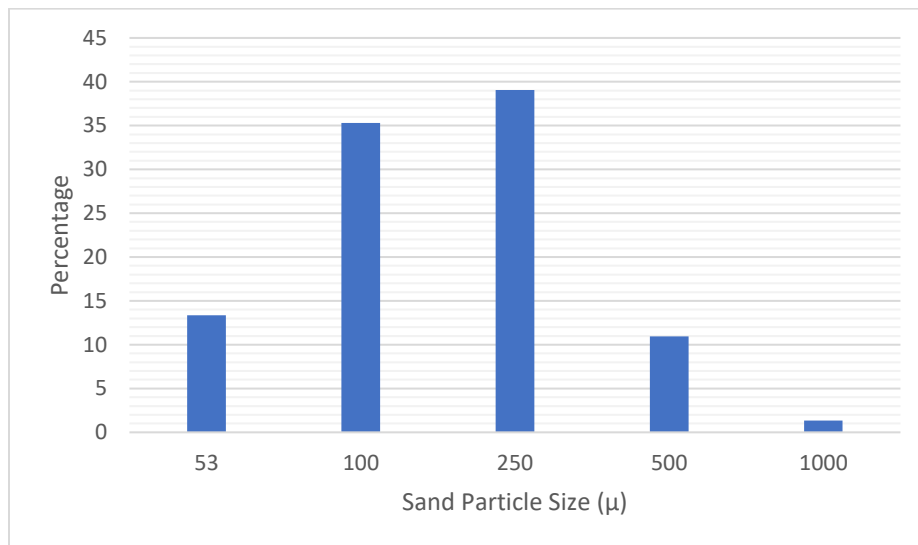


Figure B-1. Particle size distribution graph of the sand grains of the Auger 120 sample.

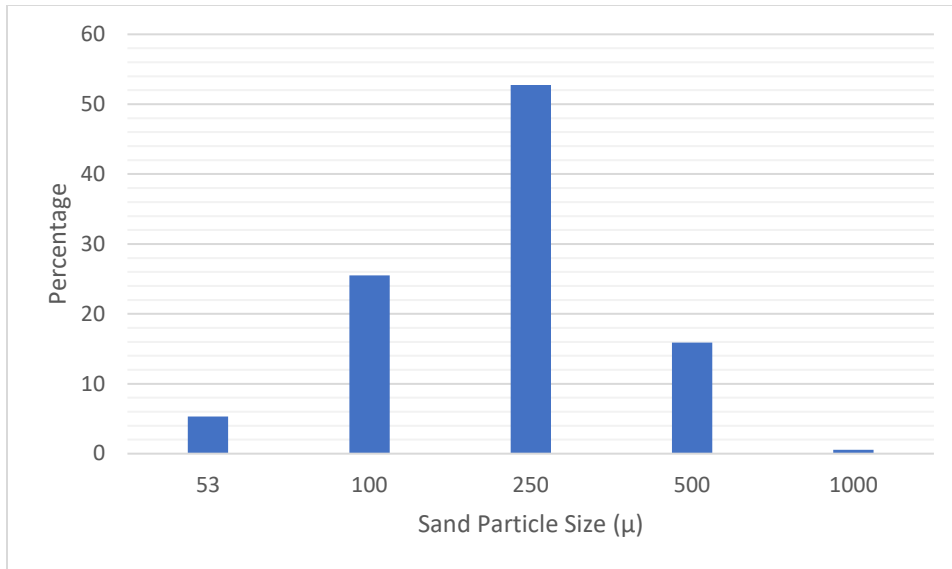


Figure B-2. Particle size distribution graph of the sand grains of the Auger 150 sample.

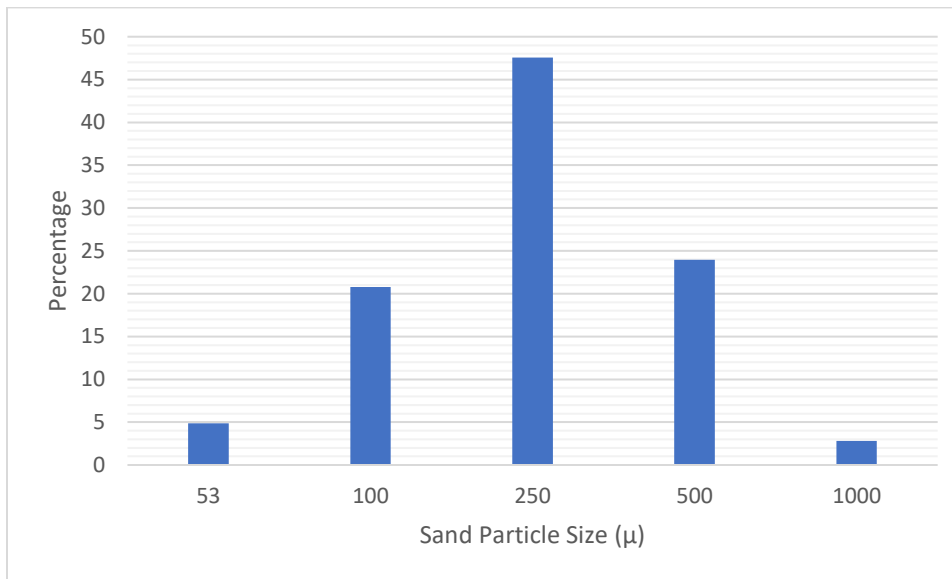


Figure B-3. Particle size distribution graph of the sand grains of the Auger 1100 sample.

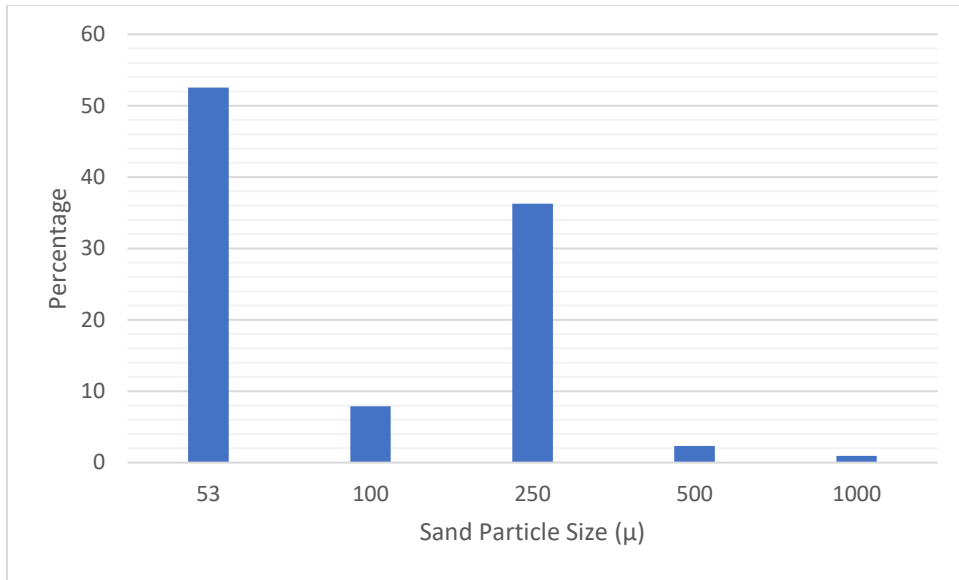


Figure B-4. Particle size distribution graph of the sand grains of the Auger 530 sample.

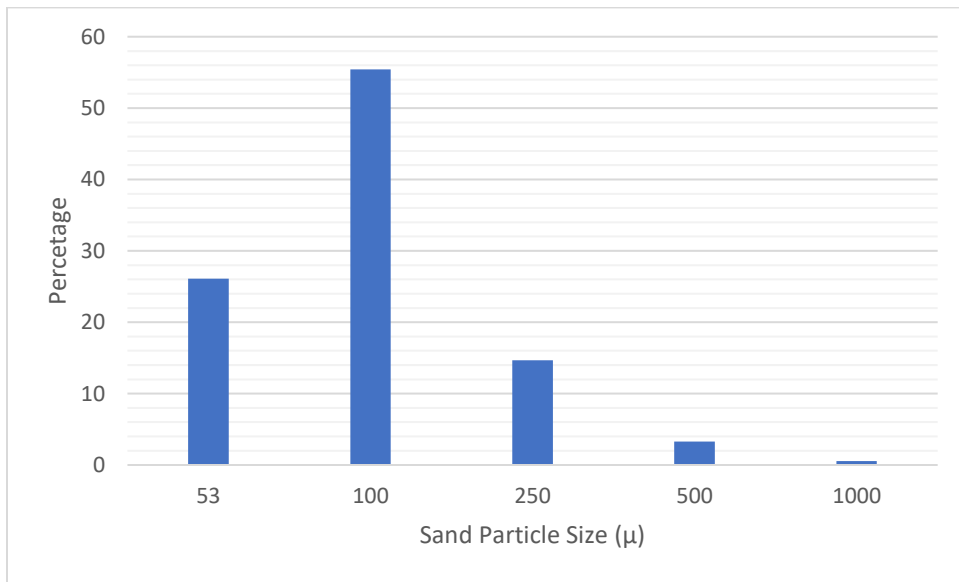


Figure B-5. Particle size distribution graph of the sand grains of the Auger 580 sample.

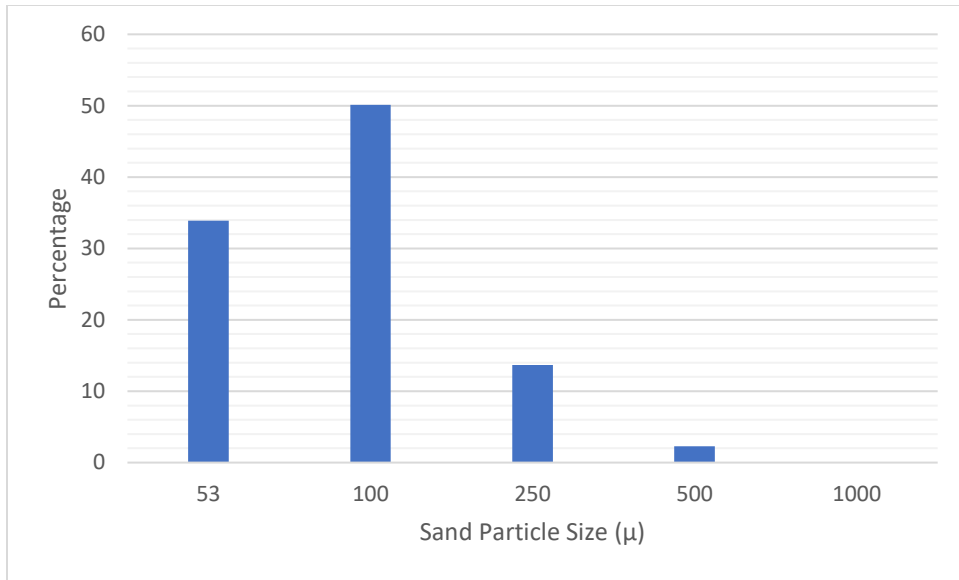


Figure B-6. Particle size distribution graph of the sand grains of the Auger 840 sample.

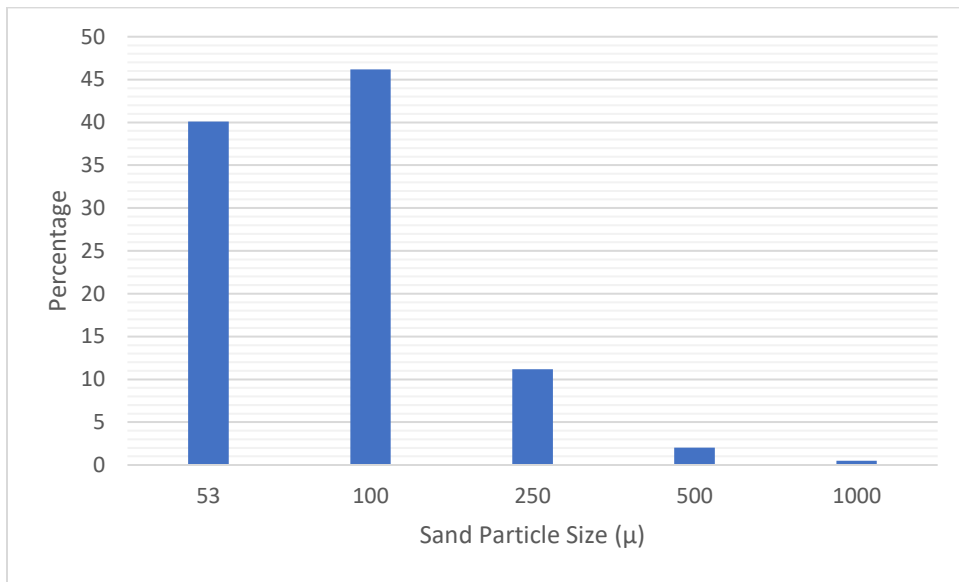


Figure B-7. Particle size distribution graph of the sand grains of the Auger 890 sample.

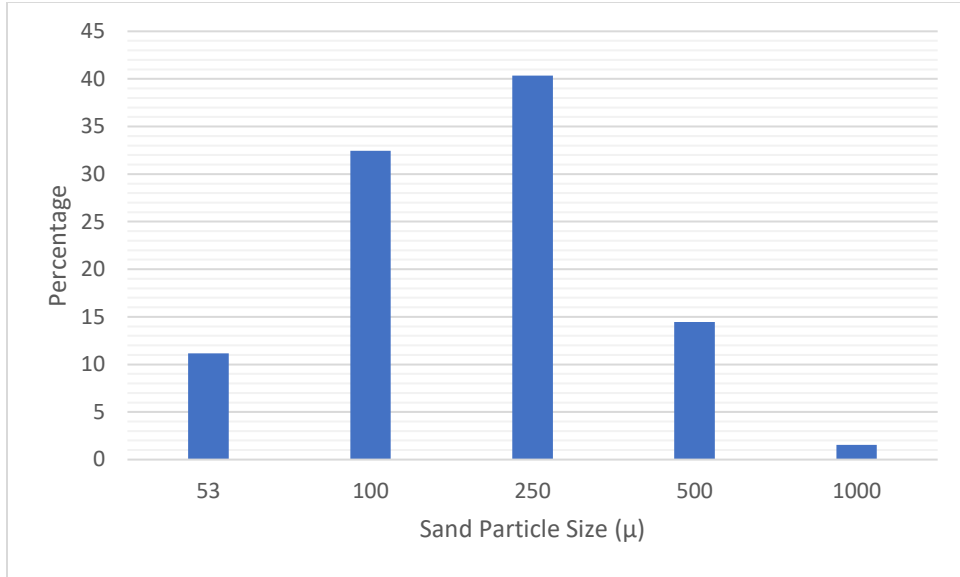


Figure B-8. Particle size distribution graph of the sand grains of the BURNS1-S sample.

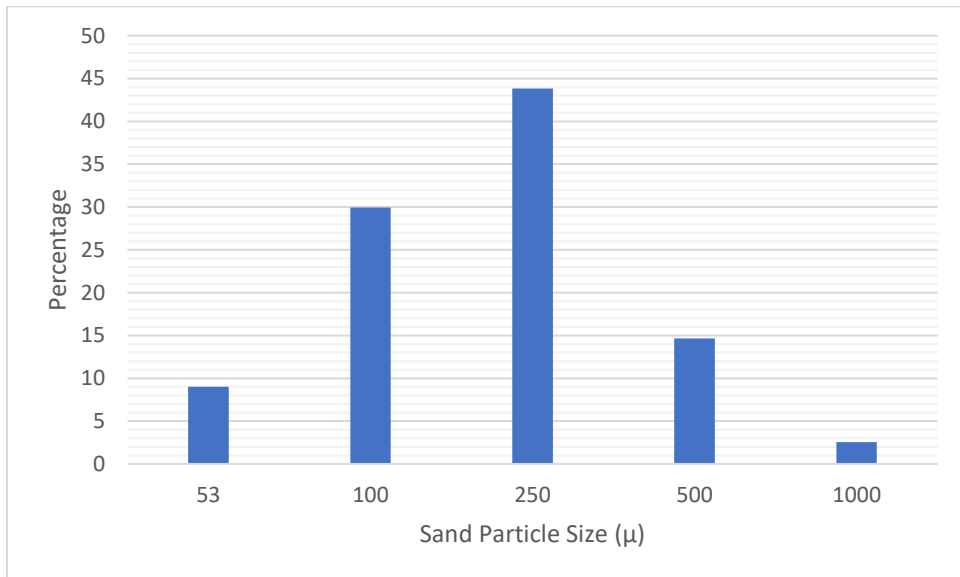


Figure B-9. Particle size distribution graph of the sand grains of the BURNS2-S sample.

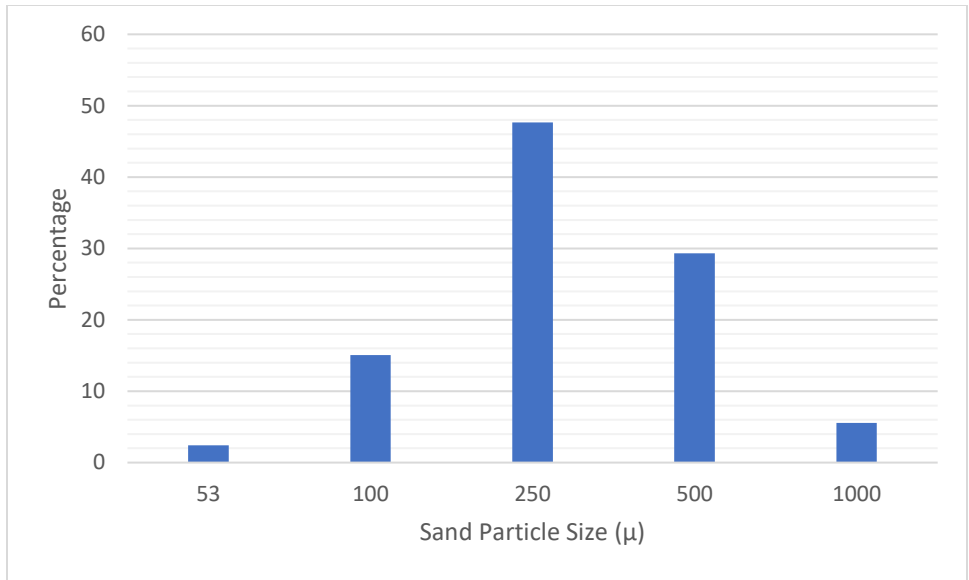


Figure B-10. Particle size distribution graph of the sand grains of the BURNS2-S sample.

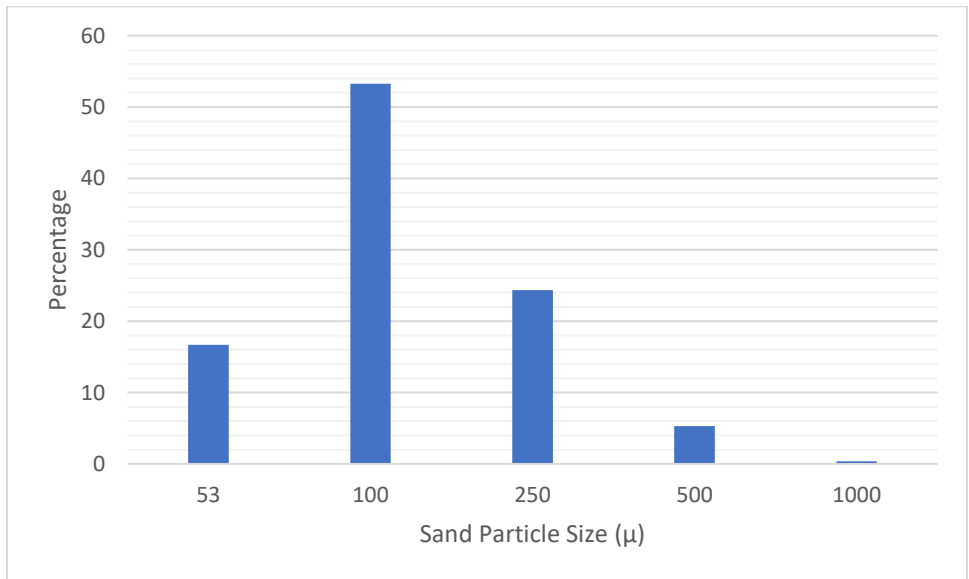


Figure B-11. Particle size distribution graph of the sand grains of the BURSS1-S sample.

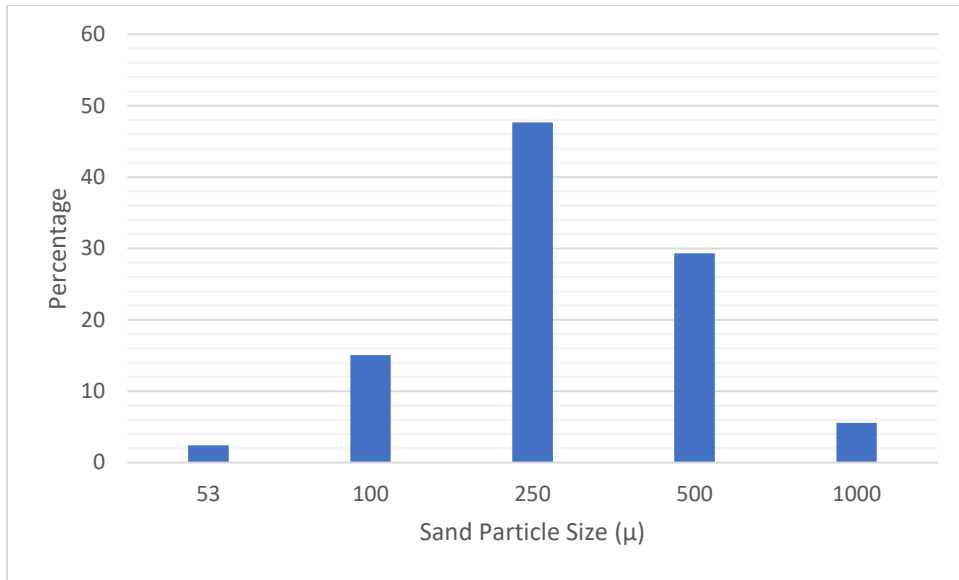


Figure B-12. Particle size distribution graph of the sand grains of the BURSS1-D sample.

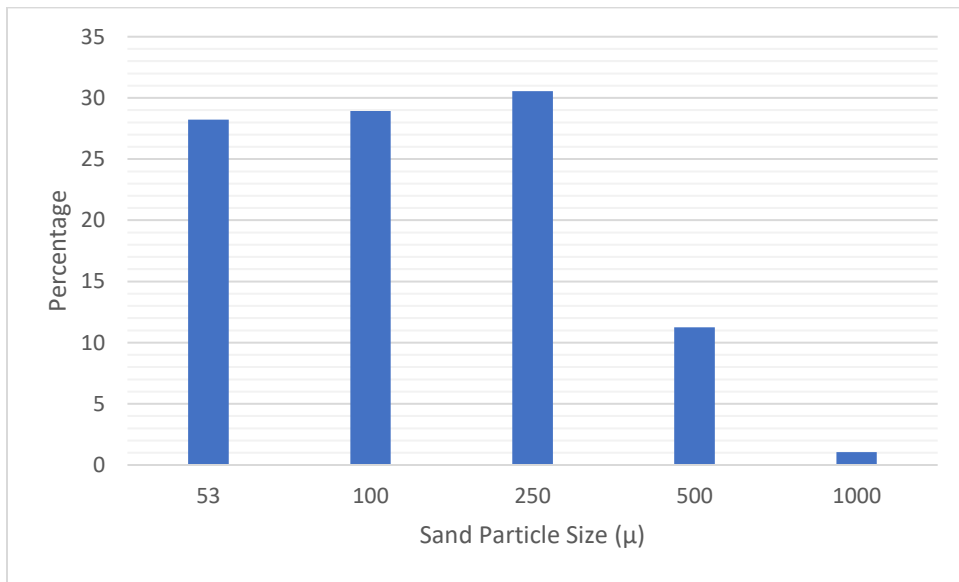


Figure B-13. Particle size distribution graph of the sand grains of the BURAN sample.

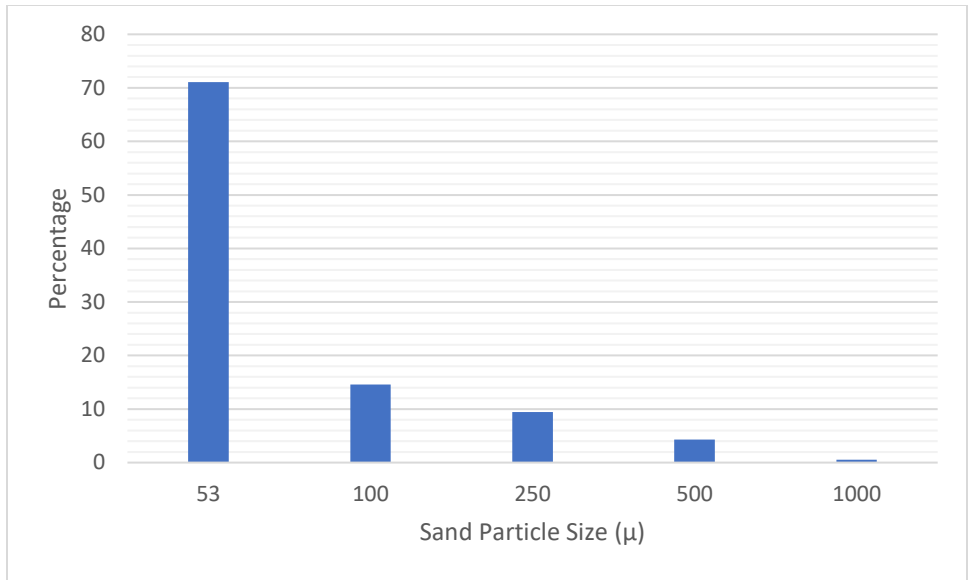


Figure B-14. Particle size distribution graph of the sand grains of the BURAM sample.

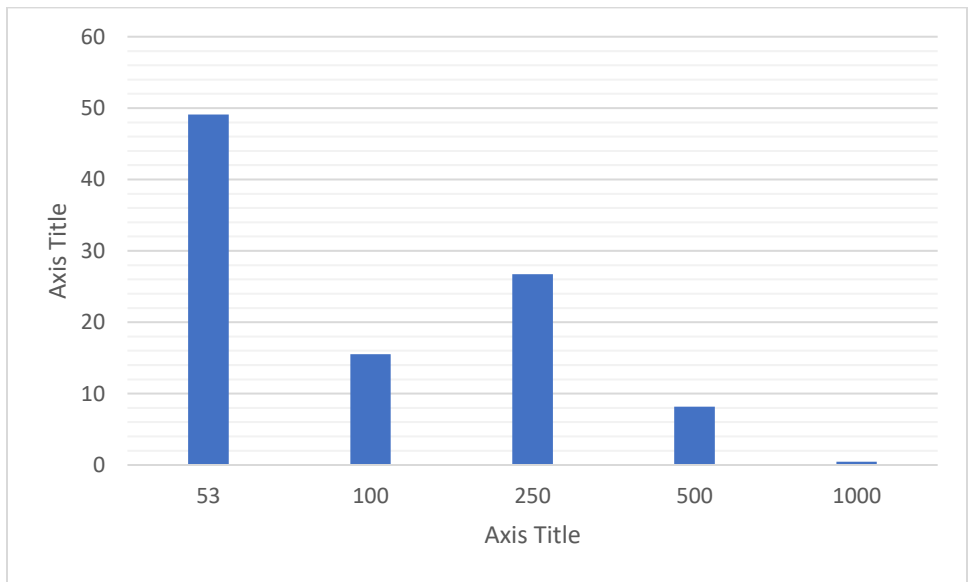


Figure B-15. Particle size distribution graph of the sand grains of the BURAS sample.

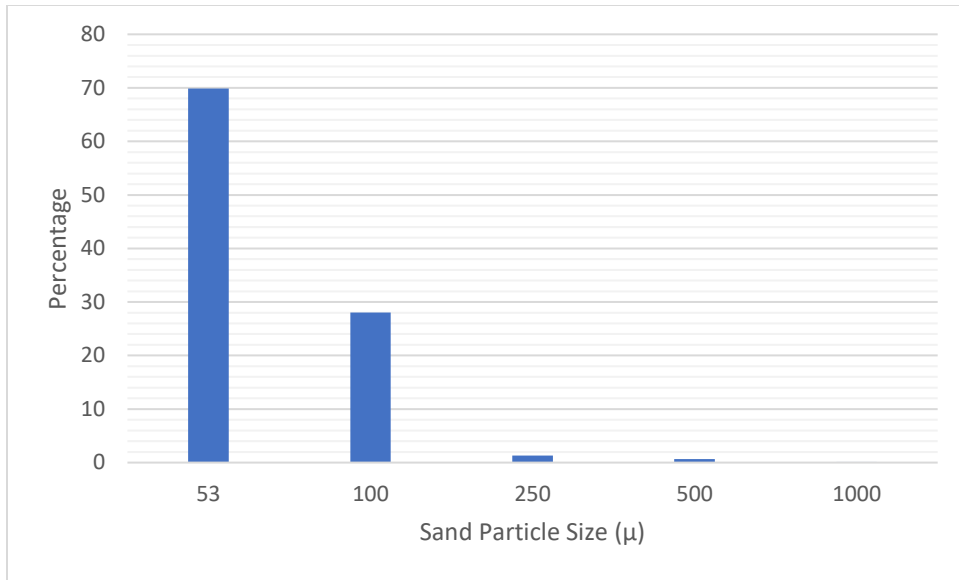


Figure B-16. Particle size distribution graph of the sand grains of the BUGS1 sample.

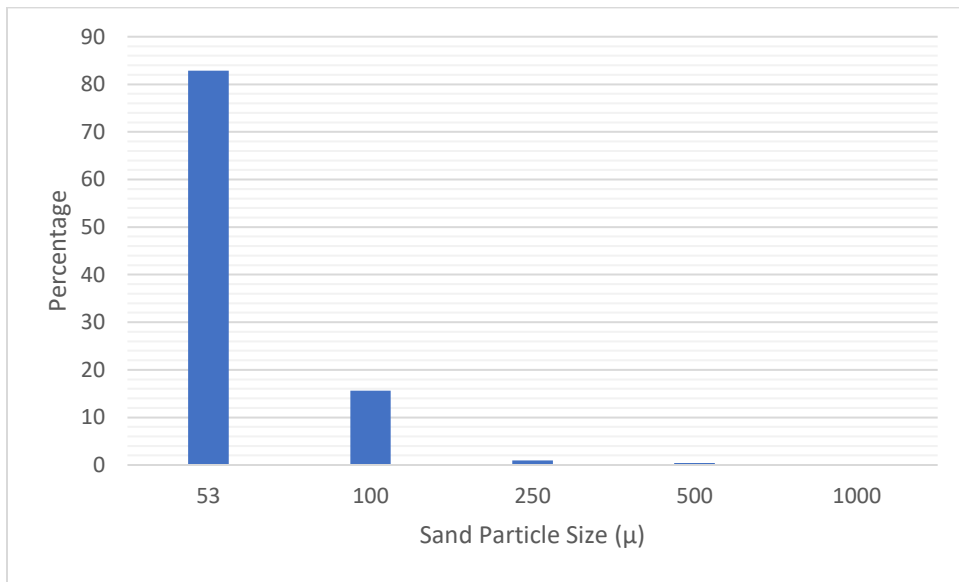


Figure B-17. Particle size distribution graph of the sand grains of the BUGR1 sample.

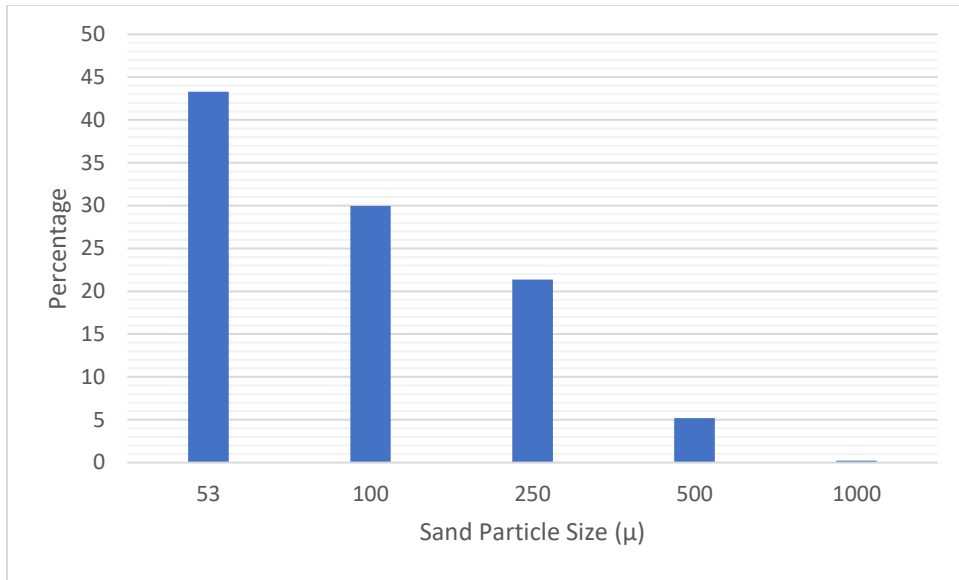


Figure B-18. Particle size distribution graph of the sand grains of the DILS1 sample.

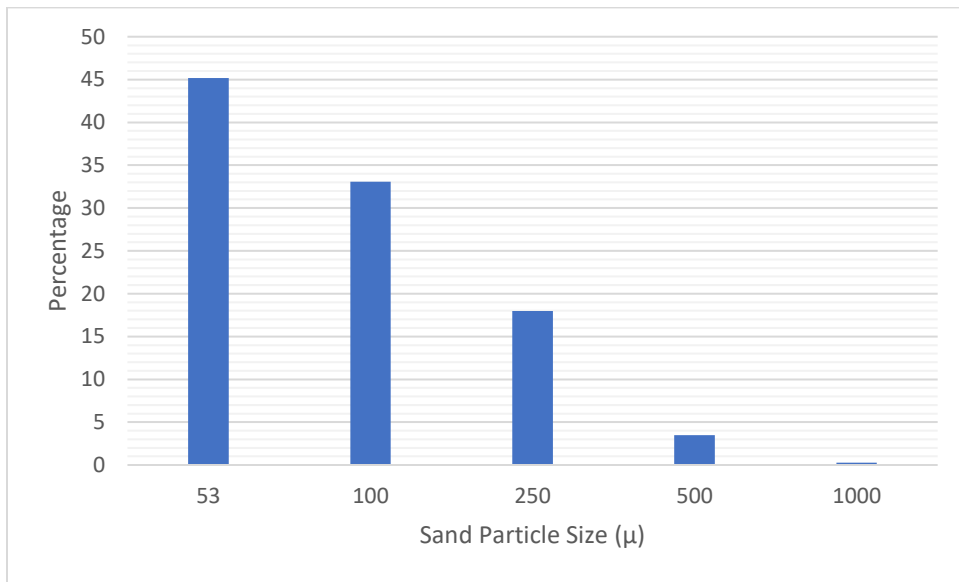


Figure B-19. Particle size distribution graph of the sand grains of the DILS2 sample.

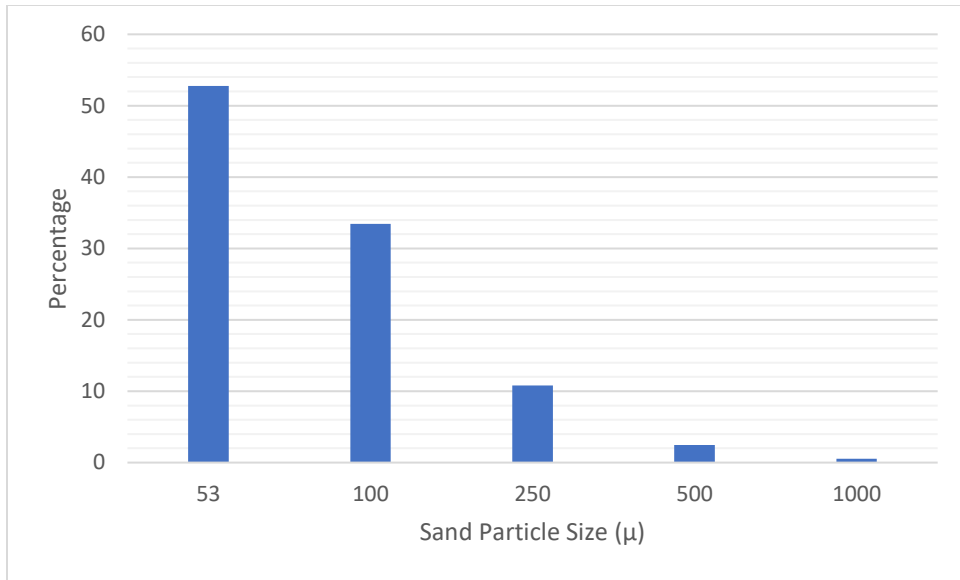


Figure B-20. Particle size distribution graph of the sand grains of the DILR1 sample.